applied sciences

MDPI

Article

Finite Element Analysis of the Thermo-Mechanically Coupled Wheel–Rail Contact Response Under Rolling and Full-Slip Conditions

Weiguo Meng, Xiaojie Sun *, Quansheng Gao and Tongkun Xu

Faculty of Intelligent Technology, Shanghai Institute of Technology, Shanghai 201418, China; 17835601753@163.com (W.M.); louise710825@163.com (Q.G.); xtongkun@163.com (T.X.)
* Correspondence: sxjlm@sit.edu.cn

Featured Application

The quantified comparison of rolling and full-slip wheel–rail contact responses under a unified thermal boundary can support slip damage analysis, rail-burn prevention, and operational safety assessment of metro vehicles subject to frequent starting and braking.

Abstract

During frequent starting and braking of metro vehicles, wheel–rail contact may change from pure rolling to full slip, and the frictional heat generated at the interface can induce localised rail damage such as rail burns. Because the motion state and the thermal input vary together in service, their separate contributions to the contact response are difficult to identify. To separate them, a three-dimensional elastic–plastic finite element model of a Type B metro wheel and rail was established and four cases were computed, forming a 2×2 factorial combination of two motion states (pure rolling and full slip) and two thermal states. The temperature field was imposed as a prescribed railhead boundary rising from 22 °C to 50 °C, applied identically under both motion states as a control variable, rather than solved from frictional heating. Under an 80 kN wheel load, the maximum rail equivalent stress of the four cases is 541.9, 596.3, 623.1 and 679.5 MPa, all exceeding the 457 MPa yield strength of U71Mn rail steel and indicating shallow localised plasticity in the contact patch. Full slip changes the peak contact pressure by less than 2% but raises the maximum rail equivalent stress by 14–15%, because the interface passes into full sliding and the high-stress zone moves towards the rail surface; the 28 °C temperature rise concentrates the contact and raises the stress by a further 9–10%. The factorial interaction term is +2.0 MPa, below 4% of either main effect. An analytical estimate shows the imposed thermal load to be a conservative lower bound for continuous sliding.

Keywords: wheel–rail contact; full slip; thermo-mechanical coupling; contact pressure; equivalent stress; finite element analysis

Check for updates

Academic Editor: Dario Croccolo

Received: 22 July 2026
Revised: 2 September 2026
Accepted: 3 September 2026
Published: 4 September 2026

Copyright: © 2026 by the authors. Licensee MDPI, Basel, Switzerland. This article is an open access article distributed under the terms and conditions of the Creative Commons Attribution (CC BY) license.

1. Introduction

Increasing intensity of rail traffic and increasing train speeds are straining the infrastructure and accelerating its deterioration. Insufficient maintenance can have significant consequences, including train derailments and broken rails [1]. Wheel–rail contact is the key link through which rail vehicles realise load carrying, traction, braking, and guidance [2,3]. Because the actual contact area between the wheel tread and the railhead is very small, the

interface sustains very high local contact pressure together with tangential friction, micro-slip, and elastic–plastic deformation of the near-surface material. During starting, braking, curve negotiation, and changes in adhesion conditions, the contact state may change from nearly pure rolling to rolling–sliding contact, and local or full sliding can occur under abnormal states such as wheel spin or locked-wheel skidding [3–5]. Sliding intensifies tangential friction and stress concentration at the interface and can induce surface-layer damage such as wear, rail burns, spalling, and rolling contact fatigue, thereby affecting running stability and the service life of wheels and rails [6–8]. Studying the stress, pressure, and friction responses of the contact zone under different motion states is therefore of great significance for revealing local damage mechanisms and ensuring operational safety.

During rolling–sliding or sliding, the frictional work done at the interface is converted into heat that accumulates near the contact zone, causing a local temperature rise and temperature gradients. The temperature field not only changes the thermal expansion state and near-surface deformation of the material but also produces additional thermal stress, which acts together with the mechanical contact stress and alters the distributions of equivalent stress, contact pressure, and friction stress in the contact zone [9–12]. Previous studies have shown that frictional heating in wheel–rail sliding significantly affects the temperature field, stress field, and residual deformation of the contact zone; when the slip is large or long-lasting, the local temperature rise may even cause microstructural changes and thermal damage [13–15]. An analysis restricted to purely mechanical contact therefore cannot fully reflect the contact response once the temperature field is involved.

Extensive research has been devoted to wheel–rail frictional heating and thermo-mechanical coupling. Regarding temperature-rise calculation and thermo-mechanical modelling, Knothe and Liebelt [4] established a method for calculating wheel–rail temperatures in sliding contact; Zhao et al. [5] solved the thermo-elastic stress of wheel–rail contact under full sliding; Wu et al. [6] and Li et al. [7,8] developed thermo-elastic and thermo-elasto-plastic finite element models and showed that increasing creepage markedly raises the surface-layer temperature rise and thermal strain of the rail; Naeimi et al. [9] built a three-dimensional elastic–plastic thermo-mechanical model to compute the flash temperature and stress–strain response of the contact zone. Regarding slip conditions and damage evolution, Srivastava et al. [10] and Lian et al. [11] analysed rail temperature, stress distribution, and fatigue and wear behaviour under various slip conditions; Yang et al. [12] considered temperature-dependent material properties and multiple heat-transfer paths and studied the influence of axle load and sliding velocity; Wu et al. [13] reproduced the formation of the martensitic white etching layer in rail steel through laboratory thermal simulation, and Wang et al. [14] experimentally revealed the competition between wear and rolling contact fatigue at different slip ratios. Regarding engineering scenarios and validation, Wei and Wu [15] and Han et al. [16] analysed the thermo-mechanical characteristics of sliding wear and of sliding contact in turnout areas, respectively; Wei et al. [17] analysed rail temperature-rise characteristics and material fatigue damage at different contact slip ratios; Zhang et al. [18] compared the accuracy and efficiency of the moving-heat-source and thermo-mechanical coupling methods for computing frictional temperature rise; He et al. [19] established a thermo-mechanically coupled model whose contact-temperature prediction was validated by high-slip experiments.

Recent international work has extended these lines in four directions of direct relevance here. First, on full-slip and high-creepage contact, Wei et al. [20] computed the railhead surface temperature and the resulting damage characteristics during sliding of a wheel under emergency braking, and Li et al. [21] extended the thermo-mechanical coupling analysis to the slip generated by hunting motion. Second, on temperature-dependent friction, Zhang and Zuo [22] showed that replacing a constant friction coefficient by a

variable of one appreciably changes the predicted thermo-mechanical behaviour of the wheel tread across operating conditions, and Huang et al. [23] introduced surface roughness and temperature into a three-dimensional adhesion model. Third, on rail thermal damage and its experimental characterisation, He et al. [24] measured the wear and damage behaviour of U71Mn rail steel over a range of ambient temperature and humidity, and Zhou et al. [25] did so under alternating temperature conditions. Fourth, on the validation of thermo-mechanical finite element models, He et al. [19] validated a wheel–rail thermo-mechanical model against infrared thermography up to contact temperatures of 360 °C; Sahoo et al. [26] inverted a measured wheel-tread temperature rise to estimate contact forces and wear number, and Tran et al. [27] reviewed the applicability and the limitations of thermal railway wheel models as a class. Taken together, this recent body of work confirms that the temperature field is now routinely treated as an active participant in the wheel–rail contact response, and that its experimental validation remains the principal open difficulty.

In summary, existing studies have concentrated on wheel–rail frictional heating, rolling–sliding contact, wear evolution, and creepage effects, providing an important basis for analysing rail thermal damage and contact fatigue. However, the differences in contact response between rolling and full slip and the changes in contact pressure, friction stress, and equivalent stress with and without the imposed thermal field still lack a quantitative comparison under unified conditions; in the frequent starting/braking scenarios of metro vehicles, rolling, local slip, and full slip may all occur, and analysing a single motion state or a single thermal input cannot reflect the differences in local contact response among conditions.

Motivated by this, the present study addresses that gap by means of a controlled factorial comparison rather than by adding one more thermo-mechanical model of a single sliding condition. A three-dimensional elastic–plastic finite element model of a single wheel and a single rail of a Type B metro vehicle is established, and four cases are computed that form a complete 2×2 factorial combination of two motion states (pure rolling and full slip) and two thermal states (no thermal load and a prescribed railhead temperature rise from 22 °C to 50 °C). The same thermal boundary is deliberately applied under both motion states as a control variable, so that the contribution of the motion state and the contribution of the temperature field can be separated and quantified independently, together with the interaction between them.

The novelty of the study therefore lies not in the thermo-mechanical formulation itself, which follows established practice, but in the design of the comparison. In the existing literature the motion state and the thermal input are almost invariably varied together: raising the creepage simultaneously raises the tangential traction and the frictional heat generation, so that the reported change in the contact response is the sum of two effects that cannot be separated afterwards. By imposing an identical thermal boundary under two different motion states, the present design breaks that confounding and yields three quantities that a single-case analysis cannot provide: the main effect of the motion state at a fixed thermal state, the main effect of the thermal load at a fixed motion state, and the interaction term between them. These are reported for the contact pressure, the friction stress and the rail equivalent stress, and are supported by positioning the four cases on the shakedown map and by an analytical estimate that places the imposed thermal load relative to the heat that continuous full sliding would actually generate. The aim is to provide a reference for wheel–rail slip damage analysis, rail-burn prevention and operational safety assessment.

2. Thermo-Mechanical Coupling Model of Wheel–Rail Contact

Wheel–rail contact involves normal contact, tangential friction, frictional heat generation and transfer, and the structural response under the temperature field. This section presents the contact and frictional heat generation model, the heat conduction model, and the evaluation indicators of the coupled response.

2.1. Contact and Frictional Heat Generation Model

Wheel–rail contact is a typical locally nonlinear contact problem. Under vertical load, local contact pressure develops in the contact zone; when relative slip exists, tangential friction stress arises simultaneously at the interface. In this paper the problem is solved by the three-dimensional finite element method, and the normal contact pressure is obtained by the contact algorithm rather than prescribed by the Hertz analytical solution. The augmented Lagrangian method is adopted for normal contact, and the contact pressure p_n is expressed as

$$p_n = \begin{cases} \varepsilon_n |g_n| + \lambda_n, & g_n \le 0 \text{ (contact)} \\ 0, & g_n > 0 \text{ (separation)} \end{cases} \quad (1)$$

where g_n is the normal contact gap, ε_n is the normal contact stiffness, and λ_n is the Lagrange multiplier term.

Tangential contact follows the Coulomb friction model, distinguishing the stick and slip states:

$$\begin{cases} \|\tau\| < \mu p_n, & \text{stick } (v_s = 0) \\ \tau = -\mu p_n \frac{v_s}{\|v_s\|}, & \text{slip } (v_s \ne 0) \end{cases} \quad (2)$$

where τ is the tangential friction stress, μ is the friction coefficient, and v_s is the wheel–rail relative slip velocity. To distinguish rolling from sliding, the longitudinal creepage is defined as

$$s = \frac{2(v - \omega r)}{(v + \omega r)} \quad (3)$$

where v is the translational velocity of the wheel, ω is its angular velocity, and r is the rolling radius. In ideal pure rolling, $s \approx 0$ and the interface is dominated by adhesion with only local micro-slip; in full slip the wheel rotates about its axle without corresponding forward motion of the contact point, the interface enters full sliding, and the tangential friction stress reaches its saturation value $\|\tau\| = \mu p_n$.

The sign conventions of Equations (1)–(3) are stated explicitly here. The normal gap g_n is measured along the outward normal of the target surface and is taken positive for separation and negative for penetration, so that the contact branch is $g_n \le 0$. The contact pressure p_n is defined positive in compression, and the penalty contribution is accordingly formed from the magnitude of the gap, $\varepsilon_n |g_n|$, which guarantees $p_n \ge 0$ throughout the contact zone and $p_n = 0$ upon separation. The term λ_n is the Lagrange multiplier contribution of the augmented Lagrangian scheme; it is updated iteratively so that the converged penetration is brought below the tolerance without requiring an arbitrarily large penalty stiffness ε_n.

The relative slip velocity v_s is the velocity of the contactor surface point relative to the coincident target surface point, resolved in the tangent plane. The frictional traction acts on the contactor surface and opposes this relative motion, which is the origin of the negative sign in the slip branch of Equation (2); the frictional power is then $\tau \cdot v_s = -\mu p_n \|v_s\|$, negative definite as Coulomb friction requires. In the stick branch the traction is a reaction determined by the constraint $v_s = 0$, and only its magnitude is constrained by $\|\tau\| < \mu p_n$, so that no direction needs to be assigned to it.

In Equation (3) the creepage is referred to the mean of the two surface velocities rather than to the wheel translational velocity alone, so that the definition remains bounded over the whole range of motion states considered here: it gives s = 0 in ideal pure rolling and s = −2 in the full-slip limit, in which the contact point does not advance and v = 0. Referring the creepage to v alone, as is usual when only small creepages are of interest, would make the definition singular in that limit.

It should be noted that the motion state referred to in this paper as full slip denotes full longitudinal sliding, in which the wheel rotates about its axle while the contact point does not advance along the rail. This is an idealised full-slip condition. It is distinct from spin creepage in the classical railway contact mechanics sense, which denotes the angular slip velocity about the contact normal and arises mainly during curve negotiation and in the presence of a wheel–rail contact angle. Throughout this paper the terms pure rolling and full slip are used consistently for the two motion states, and the term spin creepage is not used. This usage follows standard railway contact mechanics practice, in which the creepages are resolved into longitudinal, lateral and spin components and spin denotes the angular slip velocity about the contact normal [28]. The motion state analysed here has been examined previously under the description of a wheel sliding completely on the rail without advance of the contact point [29], which is kinematically identical to the full-slip condition adopted in this paper.

The frictional work done at the sliding interface is converted into heat. The frictional heat flux q and its partition between wheel and rail can be written as [4,6]

$$q = \eta\, \mu p_{\mathrm{n}} \|v_{\mathrm{s}}\|, \qquad k_q = \frac{\sqrt{(\lambda\rho c)_{\mathrm{w}}}}{\sqrt{(\lambda\rho c)_{\mathrm{w}}} + \sqrt{(\lambda\rho c)_{\mathrm{r}}}} \tag{4}$$

where η is the fraction of frictional work converted into heat, taken as 0.9 [30]; k_{q} is the fraction of heat entering the wheel, and λ, ρ, and c denote the thermal conductivity, density, and specific heat, with subscripts w and r referring to the wheel and rail. With the parameters in Table 1, $k_{\mathrm{q}} \approx 0.54$, i.e., about 54% of the frictional heat enters the wheel and 46% enters the rail, consistent with the results of [4]. The friction coefficient is taken as μ = 0.3, representing a typical dry wheel–rail condition. This value is consistent with twin-disc measurements on U71Mn rail steel, which report a steady-state friction coefficient in the range 0.30–0.35 at room temperature under dry conditions [24,25]. Since the present study is restricted to a moderate temperature range (22–50 °C), the temperature dependence of μ within this range is weak, and a constant value is appropriate for the controlled comparison of the four cases. The fraction of frictional work converted into heat, η = 0.9, is likewise in line with the values commonly adopted in wheel–rail thermal analyses [4,30]; the remaining fraction is associated with the stored energy of plastic deformation and with microstructural changes in the surface layer.

Table 1. Material parameters of the wheel and rail.

Material	Density ($\mathrm{kg\cdot m^{-3}}$)	Elastic Modulus (GPa)	Poisson's Ratio	Yield Strength (MPa)	Thermal Expansion Coefficient ($\mathrm{^{\circ}C^{-1}}$)	Thermal Conductivity ($\mathrm{W\cdot m^{-1}\cdot ^{\circ}C^{-1}}$)	Specific Heat ($\mathrm{J\cdot kg^{-1}\cdot ^{\circ}C^{-1}}$)
U71Mn rail	7850	210	0.30	457	1.10×10^{-5}	30.0	480
CL60 wheel	7850	206	0.30	465	1.45×10^{-5}	44.3	442

The implications of the constant-friction assumption at higher temperatures should nevertheless be noted. Experimental evidence indicates that the friction coefficient decreases as the contact temperature rises [22,31]. Under the several-hundred-degree con-

ditions associated with sustained full sliding, a lower μ would simultaneously reduce the tangential traction and reduce the frictional heat input, so that the two effects act in opposing directions and partially compensate. A quantitative treatment of that regime would require a temperature- and velocity-dependent friction law, such as the Polach model, together with a temperature-dependent constitutive description of the material; this lies beyond the scope of the present controlled comparison and is identified as future work. More generally, the friction coefficient is a property of the tribological system rather than of the materials alone, being set jointly by the contact pressure, the sliding velocity, the surface topography and the interfacial third body; the difficulty of prescribing a single representative value and the strong dependence of the resulting friction and wear behaviour upon it are common to heavily loaded sliding pairs in machine elements generally [32].

2.2. Heat Conduction and Thermal Boundary Model

The three-dimensional transient heat conduction equation for the wheel and rail material is [12,15,16]

$$\rho c \frac{\partial T}{\partial t} = \lambda \nabla^2 T + q_V \tag{5}$$

where T is the temperature, t is the time, ∇^2 is the Laplace operator, and q_V is the volumetric heat source; equal conductivity in all directions is assumed for the isotropic steel. Convective heat exchange occurs between the non-contact surfaces and the surrounding air, with the boundary condition

$$-\lambda \frac{\partial T}{\partial n} = h\,(T_s - T_0) \tag{6}$$

where n is the outward normal of the surface, h is the convective heat-transfer coefficient, T_s is the surface temperature, and T_0 is the ambient temperature. In the coupled cases, the action of the temperature field is described jointly by a time-varying temperature boundary, contact heat conduction, and surface convection, and is used to compare the local wheel–rail response with and without the imposed thermal field.

2.3. Relation Between the Frictional Heat Flux and the Imposed Thermal Boundary

Equation (4) describes the frictional heat generated at the wheel–rail interface and its partition between the two bodies. It is important to state explicitly how this heat generation is related to the thermal load applied in the present simulations. In the two cases involving a temperature field (Cases 2 and 4), the railhead temperature history is imposed as a prescribed thermal boundary condition and is not solved from the frictional heat flux of Equation (4). Equation (4) is used here for two purposes: to identify the physical origin of the interfacial heat input, and to determine the wheel–rail heat partition factor kq, which governs how the interfacial heat would be distributed between the two bodies. The analysis therefore constitutes a thermo-mechanically coupled structural analysis performed under a prescribed thermal boundary, rather than a fully predictive simulation of frictional heating. The terminology used throughout this paper should be understood in this sense.

To assess whether the imposed boundary is physically meaningful, the temperature rise that Equation (4) would produce is estimated analytically. Two limiting situations must be distinguished, because the contact patch is stationary on the rail in full slip but migrates along the rail in rolling.

In the full-slip cases (Cases 3 and 4) the wheel rotates about its axle while the contact point does not advance, so the heat source is stationary with respect to the railhead. As reported in Section 4.3, the interfacial frictional work in the full-slip case is approximately 5000 J over an analysis time of 0.25 s, corresponding to a mean power of about 20 kW. With an effective contact patch area of about 110 mm^2, the total interfacial heat flux is

$q = P/A \approx 1.8 \times 10^8$ W·m^{-2}. Using $k_q \approx 0.54$ from Equation (4), the flux entering the rail is $q_r \approx 8.4 \times 10^7$ W·m^{-2}. For a semi-infinite solid subjected to a constant surface heat flux, the surface temperature rise is given by the classical one-dimensional solution [33]

$$\Delta T(t) = \left(\frac{2q_r}{\lambda_r}\right)\sqrt{\frac{\alpha_r\, t}{\pi}} \tag{7}$$

where $\alpha_r = \lambda_r/(\rho_r \cdot c_r) = 7.96 \times 10^{-6}$ m^2·s^{-1} is the thermal diffusivity of U71Mn from Table 1. Substituting q_r and $t = 0.25$ s gives a railhead temperature rise in the order of 4×10^3 °C. This value exceeds the melting point of rail steel, which indicates that in reality the process would be limited by melting, phase transformation, and the associated collapse of the friction coefficient. It is nevertheless consistent with the widely reported observation that sustained full sliding produces contact temperatures of several hundred degrees and can generate the martensitic white etching layer characteristic of rail burns [7,8,13,18,19,34]. The prescribed 28 °C rise used here corresponds to an equivalent heat flux of about 5.3×10^5 W·m^{-2}, that is, to less than 1% of the flux that Equation (4) predicts for continuous full sliding.

In the rolling cases (Cases 1 and 2) the creepage is nominally zero; no net tangential force is transmitted across the interface (Section 4.2), and frictional dissipation arises only from the micro-slip within the contact patch; the corresponding heat generation is orders of magnitude smaller than in full sliding. In addition, the contact patch migrates along the rail at 22.22 m·s^{-1}, so that any given point of the railhead lies within the contact for only $t_{res} = 2a/v \approx 5.8 \times 10^{-4}$ s, with a Péclet number $Pe = va/(2\alpha_r) \approx 8.9 \times 10^3$. Even if the full-sliding heat flux derived above was applied for this residence time, the resulting flash temperature rise would be about 2×10^2 °C, and for the micro-slip levels actually present in pure rolling it is negligible.

These two estimates lead to the interpretation adopted in this study. The prescribed 22–50 °C railhead boundary is not a prediction of the self-generated contact temperature in either case; it is an externally imposed thermal load, representing a moderately heated railhead that may result from preceding braking cycles, previous traction events, or solar heating. It is applied identically in Cases 2 and 4 as a deliberate control variable, so that the influence of the motion state and the influence of the temperature field can be separated within a 2×2 comparison under otherwise identical conditions. Two consequences follow and are carried through to the conclusions. First, because the true contact temperature under continuous full sliding would be far higher than the imposed value, the thermal contribution reported for the full-slip cases is a conservative lower bound. Second, because the imposed temperature rise lies well within the range in which the room-temperature material parameters of Table 1 remain applicable, the computed response is quantitatively meaningful within that range, but no quantitative extrapolation to several-hundred-degree conditions is attempted (see Section 4.3).

A fully predictive thermo-mechanical simulation, in which the temperature field is solved directly from Equation (4) together with temperature-dependent material properties, would be required to describe the extreme-sliding regime, and is identified as the subject of future work.

2.4. Evaluation Indicators of the Coupled Response

Once the thermal field is imposed, the material expands thermally. When the expansion is constrained by the surrounding material, the contact, or the boundaries, additional thermal stress arises and acts together with the mechanical contact stress on the contact-zone

response [14–16,19]. In the thermo-elasto-plastic analysis, the total strain is decomposed into elastic, plastic, and thermal parts:

$$\boldsymbol{\varepsilon} = \boldsymbol{\varepsilon}_{\mathrm{e}} + \boldsymbol{\varepsilon}_{\mathrm{p}} + \boldsymbol{\varepsilon}_{\mathrm{th}}, \qquad \boldsymbol{\varepsilon}_{\mathrm{th}} = \alpha\, \Delta T\, \boldsymbol{I} \tag{8}$$

where ε_{e}, ε_{p}, and $\varepsilon_{\mathrm{th}}$ are the elastic, plastic, and thermal strains, α is the linear thermal expansion coefficient, ΔT is the temperature change, and $\boldsymbol{I}$ is the unit tensor; the plastic branch is described by bilinear isotropic hardening. The von Mises equivalent stress is used to evaluate the material response under complex stress states:

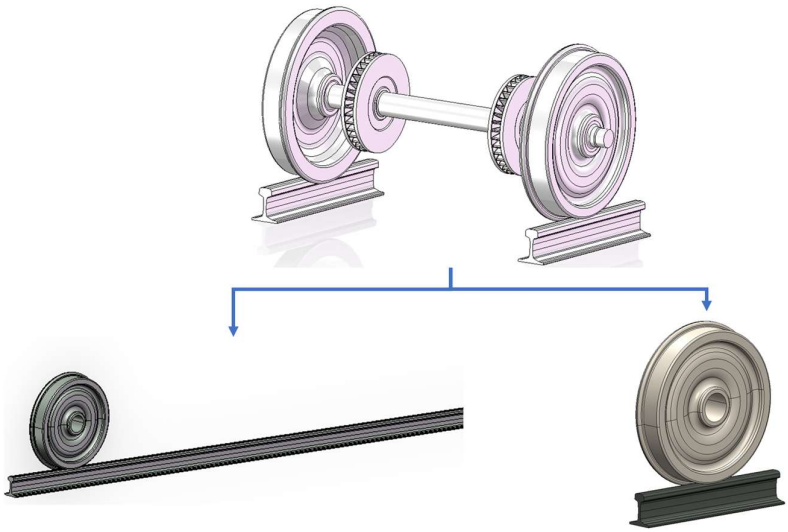
$$\sigma_{\mathrm{e}} = \sqrt{1/2[(\sigma_1 - \sigma_2)^2 + (\sigma_2 - \sigma_3)^2 + (\sigma_3 - \sigma_1)^2\ ]} \tag{9}$$

where σ_1, σ_2, and σ_3 are the principal stresses. The analysis focuses on the contact pressure, friction stress, and rail equivalent stress to compare the influence of rolling, full slip, and thermo-mechanical coupling on the local wheel–rail response.

3. Finite Element Model and Simulation Cases

3.1. Geometric Model and Simplifications

To analyse the local thermo-mechanical response of the contact zone in rolling and full slip, a three-dimensional finite element model of a single wheel and a single rail is established. Since a complete wheelset–track model is computationally expensive and this study focuses on the local response of one-side contact under tangent-track conditions, the system is simplified to one wheel in contact with one rail. The simplification retains the main geometric features of the tread, the railhead, and the contact interface while reducing the model size, and is suitable for comparing contact responses under different motion states and thermal inputs. According to the motion characteristics of the cases, a long-rail rolling model and a short-rail full-slip model are used: the rolling cases use a longer rail so that the contact position migrates continuously along the rail, whereas the full-slip cases use a shorter rail with the wheel rotating about its axle within a local contact zone. Contact is defined between the wheel tread and the railhead, and the rail base is fixed to represent the support of the substructure, as shown in Figure 1.



(a) Rolling model (b) Full-slip model

Figure 1. Geometric model of the wheel–rail finite element system, simplified from the full wheelset (top): (**a**) rolling model with a long rail; (**b**) full-slip model with a short rail.

The wheel is modelled with the LM tread profile and a nominal diameter of 840 mm (rolling radius of 420 mm), corresponding to a new wheel of a Type B metro vehicle. The rail is a Chinese 60 kg·m^{-1} rail (CHN60) with a railhead crown radius of 300 mm, laid at a cant of 1:40. This LM/CHN60 pairing is the standard wheel–rail profile combination used in Chinese metro systems [31,35]. The rolling model uses a rail length of 15,000 mm so that the contact position can migrate continuously along the rail, whereas the full-slip model uses a shorter rail of 1000 mm, since the contact patch remains stationary in that case.

The limitations that follow from this simplification should be stated explicitly. The model represents one wheel and one rail on tangent track, and therefore omits the wheelset and axle, the adjacent wheelsets, the primary and secondary suspension and the car body, the discrete support provided by fasteners, sleepers and ballast, and the associated track dynamics. The vertical load is consequently applied as a static equivalent, and the dynamic wheel–rail force fluctuation caused by vehicle and track vibrations is not reproduced, nor are the lateral force, the angle of attack and the spin creepage that develop during curve negotiation, where rotational slip is most pronounced. The rail base is fully constrained, which represents a rigid foundation: this idealisation suppresses the global bending and the longitudinal thermal expansion of the rail and therefore maximises the constraint on the thermal strain of the railhead. Its influence is quantified in Section 4.3, where the computed thermal-stress slope is shown to be about 85% of the fully constrained theoretical value, so that the thermal stress reported here is an upper estimate of what a compliant support would give at the same temperature rise. Finally, the tread and the railhead are modelled as geometrically perfect and smooth. Real running surfaces carry micro-roughness, corrugation and local defects, which redistribute the pressure within the patch and can raise the local peak pressure well above the smooth-surface value; recent adhesion models that resolve roughness and temperature together show this explicitly [23]. The present results should therefore be read as the response of a nominally smooth interface, and not as an upper bound on the local contact pressure.

These simplifications are acceptable here because the object of the study is a controlled comparison rather than an absolute prediction. All four cases share the same geometry, the same support condition, the same mesh and the same load, so that the simplifications act identically in every case and cancel in the differences between cases, which are the quantities on which the conclusions are based. The absolute stress levels reported below are correspondingly specific to the idealised configuration analysed, and transferring them to a particular vehicle–track system would require the neglected effects to be reinstated.

3.2. Material Parameters and Constitutive Model

The wheel is made of CL60 wheel steel and the rail of U71Mn rail steel. The mechanical behaviour is described by isotropic elasticity combined with bilinear isotropic hardening. Beyond the yield strength, the stress–total-strain relation continues along a straight line whose slope is the post-yield tangent modulus, taken for the U71Mn rail steel, which carries all of the plastic response reported below, as E_t = 2.0 GPa. The resulting hardening rate is modest, where $E_t/E \approx 1/105$, and the computed flow stress therefore remains well below the tensile strength of 880 MPa specified for this grade in TB/T 2344.1-2020 [36] over the whole range of plastic strain reached in the simulations (Section 4.2). The cases involving a thermal load additionally require the thermal conductivity, specific heat and thermal expansion coefficient. The main parameters are listed in Table 1.

The material parameters listed in Table 1 are representative values for U71Mn rail steel and CL60 wheel steel of the type commonly adopted in wheel–rail thermo-mechanical finite element analyses, and were not measured in the present study. The steel grades correspond to TB/T 2344.1-2020 [36] (U71Mn rail) and TB/T 2708-2023 [37] (CL60 wheel);

since these standards specify tensile rather than yield strength, the yield values used here are representative literature values for the as-rolled condition. The rail thermal expansion coefficient of 1.10×10^{-5} °C^{-1}, which governs the thermal response reported in this study, is consistent with the published values for rail steel [31]. The heat partition factor of Equation (4) serves only to identify the physical origin of the interfacial heat: because the temperature field is imposed as a prescribed boundary (Section 2.3), it does not enter the computation, and the order-of-magnitude estimate given in that section is unchanged for heat partition factors over the range of 0.46–0.52.

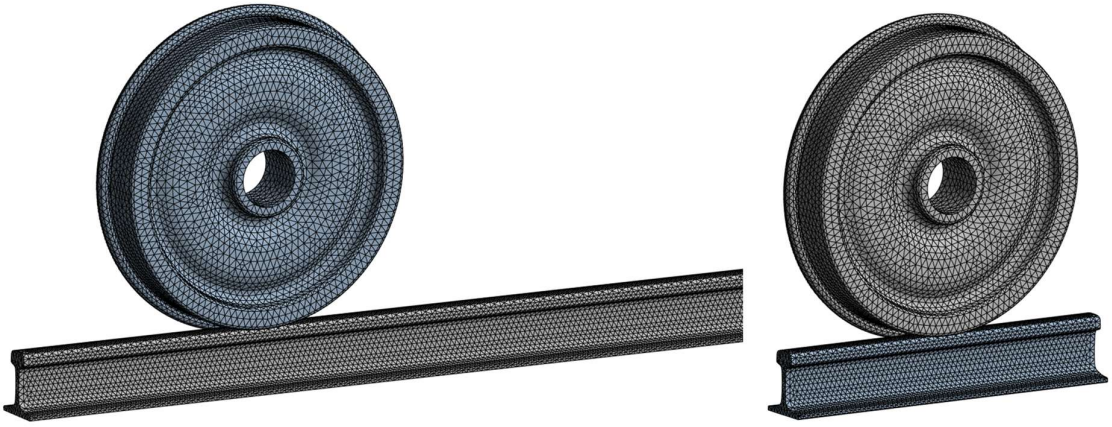
The applicable temperature range of the room-temperature parameters in Table 1 can be stated quantitatively using published temperature-dependent data for rail steel [31]. Over the 22–50 °C interval spanned by the thermal boundary imposed here, that data set gives an elastic modulus falling from about 209 GPa at 25 °C to about 207 GPa at 100 °C, a change below 1%; an unchanged yield strength over the same interval; a friction coefficient decreasing from about 0.334 to about 0.301, so that the change within 22–50 °C is below 4%; and a linear thermal expansion coefficient rising from 11.0×10^{-6} to 11.6×10^{-6} °C^{-1}, at about 5%. The absolute values of that data set differ from those of Table 1—its room-temperature yield strength is 608 MPa—so they are used here only for the relative temperature dependence, which is the quantity of interest. Of the four properties, the expansion coefficient shows the largest variation and enters the thermal strain linearly, so the associated uncertainty in the computed thermal stress is of the same order, at about 5%. That is small compared with the 9–10% thermal effect reported in Section 4.2 and does not alter the ranking of the four cases.

Outside that interval the same data show the parameters departing rapidly from their room-temperature values: at 650 °C the elastic modulus has fallen to about 105 GPa, a reduction of 50%, the yield strength to about 502 MPa, a reduction of 17%, and the friction coefficient to about 0.139, a reduction of 58% [31]. Compression tests on U71Mn rail steel over 20–800 °C likewise show a marked reduction in flow stress with increasing temperature [38]. The room-temperature parameter set of Table 1 is therefore quantitatively adequate for the moderate thermal boundary imposed in this study, but is not applicable to the several-hundred-degree conditions associated with sustained full sliding. This is the reason why no quantitative extrapolation to that regime is attempted, as stated in Sections 2.3 and 4.3.

3.3. Meshing and Mesh-Independence Verification

The wheel–rail model is discretised with three-dimensional solid elements. To balance computational efficiency and accuracy in the contact zone, the mesh is locally refined near the contact region, where the element size is reduced to about 1 mm and gradually coarsened away from it, as shown in Figure 2. The rolling model contains more elements owing to the longer rail, and the full-slip model is correspondingly smaller.

To verify that the results are independent of the mesh, the static loading step of Case 1 (80 kN vertical load) was recomputed with contact-zone element sizes of 2.0, 1.0, and 0.5 mm under otherwise identical contact algorithms, material parameters, and boundary conditions, monitoring the peak contact pressure, the effective contact patch area, and the maximum rail equivalent stress. The results are listed in Table 2.



(a) Rolling model (long rail) (b) Full-slip model (short rail)

Figure 2. Finite element mesh of the wheel–rail model: (**a**) rolling model with a long rail; (**b**) full-slip model with a short rail.

Table 2. Mesh-independence verification results.

Mesh Scheme	Contact-Zone Element Size (mm)	Total Elements ($\times 10^4$)	Peak Contact Pressure (MPa)	Contact Patch Area (mm^2)	Max. Rail Equivalent Stress (MPa)
Coarse	2.0	32	1024	117	519
Medium (adopted)	1.0	58	1088	110	541.9
Fine	0.5	152	1104	109	548

As shown in Table 2, when the mesh is refined from 2.0 mm to 1.0 mm, the relative changes in the peak contact pressure and the maximum rail equivalent stress are 6.3% and 4.4%, respectively; when it is further refined from 1.0 mm to 0.5 mm, the three indicators change by only 1.5%, 0.9%, and 1.1%, all below 3%, indicating that the 1.0 mm contact-zone mesh satisfies mesh independence. All subsequent analyses are based on this mesh.

The contact solution was further verified on this basis: repeating the static loading with a linear-elastic material, the Hertz theory—with the present geometry and load (wheel rolling radius of 420 mm, railhead crown radius of 300 mm, vertical load of 80 kN, effective modulus $E^* \approx 114.3$ GPa)—gives a peak contact pressure of about 1.17 GPa and a contact patch area of about 102 mm^2 (ellipse semi-axes of about 6.4 mm $\times$ 5.1 mm), and the linear-elastic finite element solution deviates from the theoretical values by 2.7%, validating the contact modelling and mesh scheme. The elastic–plastic peak contact pressure is lower than the elastic theoretical value because local yielding in the contact patch flattens the pressure distribution, consistent with the general behaviour of elastic–plastic contact [39].

The comparatively large change between the 2.0 mm and the 1.0 mm meshes deserves comment. The Hertzian contact patch for the present geometry and load has semi-axes of about 6.4 mm $\times$ 5.1 mm, so that a 2.0 mm element spans the full minor axis with only about five elements. At that resolution the steep pressure gradient towards the edge of the patch is under-resolved, and the discretised patch boundary can advance only in steps of one element. The two consequences appear together and with opposite signs: the pressure peak is truncated, with 1024 MPa against 1088 MPa on the 1.0 mm mesh, while the patch area is overestimated, with 117 mm^2 against 110 mm^2, the two errors being linked by the requirement that the pressure integral balances the applied load. Refining to 1.0 mm raises the count across the minor axis to about ten elements, which is the resolution generally regarded as adequate for a Hertzian-type patch, and the residual changes in further refinement to 0.5 mm fall below 1.5% for all three indicators. The difference between the 2.0 mm and 1.0 mm meshes is therefore a discretisation effect of

an insufficiently resolved contact patch, rather than an indication that convergence has not been attained; the monotonic and rapidly decaying character of the sequence—6.3% and then 1.5% for the peak contact pressure, and 4.4% and then 1.1% for the maximum rail equivalent stress—supports that interpretation. The 1.0 mm mesh was adopted because it delivers converged results at about 40% of the element count of the 0.5 mm mesh.

The convergence can be quantified beyond the pairwise differences in Table 2. The three meshes form a sequence with a constant refinement ratio of two, so that the observed order of accuracy and the discretisation uncertainty may be estimated by Richardson extrapolation and the grid convergence index [40]. The observed orders are 2.00 for the peak contact pressure, 2.81 for the contact patch area and 1.91 for the maximum rail equivalent stress. Values close to two are those expected for the quadratic solid elements used here, which indicate that the sequence lies within the asymptotic range of convergence and that the differences in Table 2 reflect discretisation error rather than an incidental clustering of results. Evaluated with the customary safety factor of 1.25, the grid convergence index of the adopted 1.0 mm mesh is 2.45%, 1.33% and 1.92% for the three quantities respectively, and the corresponding Richardson extrapolated values are 1109 MPa, 108.8 mm^2 and 550 MPa. The discretisation uncertainty of the adopted mesh is therefore below 2.5%, that is, four to six times smaller than the 8–15% differences on which the conclusions of Section 4 rest.

The mesh study was carried out on the mechanical rolling case, and its transferability to the thermo-mechanically coupled full-slip case requires comment. Three considerations apply. First, the mesh requirement in this problem is set by the resolution of the contact pressure gradient across the minor axis of the contact patch, which is a property of the normal contact solution; as reported in Section 3.7, the peak contact pressure and the patch area of the rolling and full-slip models differ by only 1.9% and about 2%, so that the normal solution which the mesh must resolve is essentially common to the four cases. Second, the temperature field here is a prescribed boundary condition rather than a field solved from a concentrated frictional heat source (Section 2.3); there is consequently no steep thermal gradient at the contact patch for the mesh to resolve, and the thermal contribution enters the mechanical problem as a body load whose magnitude is bounded by $E\alpha\Delta T$, a global quantity insensitive to the contact-zone discretisation. Third, the plastic zone in the rolling cases extends over several element layers, so that its resolution is comparable to that of the case examined above, whereas in the full-slip cases the plastic zone is concentrated at the surface and the mesh resolves its position but not its internal structure (Section 4.2). The convergence established above is therefore expected to carry over to the coupled cases, with the qualification that the depth distribution of plastic strain in full slip is resolved only to within one element layer. A direct three-mesh study of the coupled full-slip case is identified as a useful extension of the present verification.

3.4. Verification and Literature-Based Comparison

A distinction is drawn here between two levels of assessment. Verification confirms that the numerical contact algorithm and the mesh reproduce a known solution correctly; this is addressed by the mesh-independence study and by the comparison with the Hertz analytical solution presented in Section 3.3. Validation is concerned with whether the model reproduces physical behaviour reported by independent studies. Because no direct experimental measurement is available for the present configuration, validation is pursued here by comparison with independently published finite element results obtained under closely comparable conditions.

Kim and Kim [41] performed a three-dimensional elastic–plastic finite element analysis of wheel–rail rolling contact using a nonlinear kinematic hardening material model. Their

configuration is closely comparable to the present one: a railhead crown radius of 300 mm, a minimum contact-zone element size of 1 mm, a wheel diameter of 860 mm, and a wheel load of 85 kN, against 300 mm, 1 mm, 840 mm, and 80 kN in the present study. The comparison is summarised in Table 3.

Table 3. Comparison of the present model with independently published finite element results obtained under comparable conditions.

Quantity	Kim and Kim [41]	Present Study	Remark
Wheel load (kN)	85	80	comparable
Wheel diameter (mm)	860	840	comparable
Railhead crown radius (mm)	300	300	identical
Minimum contact-zone element size (mm)	1.0	1.0	identical
Hertz peak contact pressure (MPa)	1198.1	1170	2.4% difference
Hertz contact semi-axes a × b (mm)	6.54 × 5.18	6.4 × 5.1	2% difference
Elastic–plastic FE peak contact pressure (MPa)	1111.4	1088	2.1% difference
FE peak pressure relative to Hertz	−7%	−7%	identical trend
FE contact patch relative to Hertz	larger (a: +13%)	larger (area: +8%)	same direction
Change in peak pressure with tangential traction	1.7% for mu = 0 to 0.2	<2% for rolling to full slip	mutually consistent
Maximum von Mises stress vs. yield strength (MPa)	656.9 vs. 626.7	541.9 vs. 457	both exceed yield

Three points follow from this comparison. First, the elastic–plastic peak contact pressure obtained here is 7% below the Hertz elastic value, in agreement with the 7% reduction reported by Kim and Kim, and the underlying mechanism is the same: local yielding flattens the pressure distribution and enlarges the contact patch relative to the elastic solution. Second, the contact patch computed by the elastic–plastic model is larger than the Hertz prediction in both studies, which supports the patch areas reported in Section 4.1. Third, and most directly relevant to the present conclusions, Kim and Kim found that increasing the friction coefficient from 0 to 0.2 changed the peak contact pressure by only 1.7%, that is, the tangential traction has little influence on the normal contact response. This independently corroborates the finding of the present study that the change in motion state alters the peak contact pressure by less than 2% while substantially altering the rail equivalent stress.

It must be emphasised that this comparison validates the mechanical contact response only. The thermal part of the model is not validated against measurements in the present study. For reference, He et al. [19] validated a thermo-mechanical wheel–rail finite element model against infrared thermographic measurements up to contact temperatures of 360 °C and reported an approximately linear relationship between slip ratio and contact temperature, and Han et al. [42] obtained railhead contact temperatures of about 813 °C for a 30 t axle load sliding at 2 $m \cdot s^{-1}$ using a directly coupled model with temperature-dependent material properties. Both studies confirm that the contact temperatures associated with sustained sliding are far above the moderate boundary imposed here, which is consistent with the analytical estimate of Section 2.3. The absence of direct experimental validation of the thermal response is acknowledged as a limitation of the present work.

3.5. Contact and Thermal-Contact Settings

A frictional contact pair is defined at the wheel–rail interface, with the wheel tread as the contact surface and the railhead as the target surface in an asymmetric definition. The augmented Lagrangian method is used for normal contact to control penetration while maintaining the stability of the nonlinear solution; the Coulomb friction model with a friction coefficient of 0.3 is used tangentially. Because large relative displacement occurs during rolling and full slip, the small-sliding assumption is switched off; a normal

stiffness factor of 0.1 and a stabilisation damping factor of 0.01 are adopted to improve convergence. In the coupled cases, thermal contact conduction with a conductance of 5.0×10^4 W/(m^2·°C) is defined at the interface to describe the heat exchange in the contact zone; convection and radiation are applied to the exposed surfaces with an ambient temperature of 22 °C. The equivalent surface heat-transfer coefficient was estimated as follows. For the forced convection induced by the running airflow, a flat-plate correlation with a free-stream velocity of 22.22 m·s^{-1} and air properties at 22 °C ($\nu = 1.57 \times 10^{-5}$ m^2·s^{-1}, kair = 0.0263 W·m^{-1}·K^{-1}, $P_r = 0.707$) gives Reynolds numbers of 2.8×10^4 to 9.9×10^4 for characteristic lengths between 0.02 m and 0.07 m. Hence, this results in average convection coefficients of approximately 70 to 130 W·m^{-2}·K^{-1}. The radiative contribution, linearized as $h_{rad} = \varepsilon\sigma(T_s^2 + T_\infty^2)(T_s + T_\infty)$ with an emissivity of 0.8 for oxidised steel at a surface temperature of 50 °C, amounts to only about 5 W·m^{-2}·K^{-1}. The combined coefficient is therefore of the order of 10^2 W·m^{-2}·K^{-1}, and radiation is negligible compared with forced convection over the temperature range investigated; a time-varying temperature boundary is imposed on the railhead region to represent the heat input process of the contact zone.

The numerical contact parameters were selected as follows. The normal stiffness factor of 0.1 is the value recommended for contact-dominated and bending-dominated problems, in which the default unit factor produces an excessively stiff interface and impairs convergence; because the augmented Lagrangian formulation compensates a reduced penalty stiffness through the Lagrange multiplier update, the converged penetration is controlled largely, independent of the factor itself. The adequacy of this choice is demonstrated by the verification reported in Section 3.3. An insufficient normal stiffness permits excessive penetration, which enlarges the contact patch and depresses the peak pressure; yet the linear-elastic solution obtained exactly with these contact settings reproduces the Hertz peak pressure and patch dimensions to within 2.7%. A deviation of that magnitude is incompatible with a significantly over-compliant interface, so the Hertz comparison serves simultaneously as a check on the normal stiffness factor. The stabilisation damping factor of 0.01 is a convergence aid that suppresses rigid-body motion before contact is established; it introduces a viscous term proportional to the normal approach velocity, which decays as the contact closes. Its influence on the converged solution is not apparent in the computed histories, which settle to steady plateaus after the initial transient (see Section 4.1) rather than exhibiting the progressive drift characteristic of an actively dissipating stabilisation term.

The thermal contact conductance of 5.0×10^4 W·m^{-2}·°C^{-1} requires separate comment, since it is high in comparison with values measured for nominally flat metallic joints. Those measurements are obtained at nominal contact pressures of the order of 1–10 MPa, and they establish that the conductance increases with contact pressure following a power law, as the asperity contact area grows [43]. The wheel–rail interface operates at some three orders of magnitude higher, at contact pressures of the order of 1 GPa, at which the asperities are almost completely flattened and the joint approaches a metallurgically continuous interface; extrapolating the low-pressure correlations to that regime therefore underestimates the conductance substantially. Direct measurements at wheel–rail contact pressures are not available in the literature, and this is acknowledged as a source of uncertainty.

More importantly, the quantities reported in this study are insensitive to this parameter, for a reason that follows directly from the model formulation of Sections 2.3 and 3.5. The railhead temperature is prescribed as a temperature degree-of-freedom constraint, so the interfacial conductance does not determine the temperature of the heated railhead segment that drives the reported rail stresses; it governs the heat flux transmitted into the wheel, which is not a reported quantity. Furthermore, to whatever extent the conductance does influence the rail surface temperature—by allowing heat to leave the heated railhead through the interface. A larger conductance removes more heat from the rail; therefore, it

reduces the computed thermal expansion and the associated thermal stress. An overestimated conductance consequently biases the reported thermal contribution downwards rather than upwards, so that the value adopted here cannot inflate the thermal effect. A direct sensitivity study of this parameter is identified as future work in Section 5.

The analyses were carried out in ANSYS Workbench 2024 R1. The wheel and rail are discretised with three-dimensional ten-node solid elements: SOLID187 structural elements in Case 1, and SOLID227 coupled-field elements in Cases 2–4, whose nodes carry the three displacement degrees of freedom together with temperature. The two element types share the same ten-node quadratic displacement formulation, so that in the absence of a thermal load they return the same mechanical solution and the element choice does not affect the comparison between the cases. The wheel–rail interface is represented by a CONTA174/TARGE170 surface-to-surface contact pair, and the sparse direct solver is used. The two cases involving a thermal load, Cases 2 and 4, are solved as a direct coupled-field analysis: the structural and thermal fields are assembled in a single system of equations and solved simultaneously with the strong coupling option, rather than being solved in sequence and transferred between analyses. The prescribed railhead temperature described in Section 2.3 is imposed as a temperature degree-of-freedom constraint on the heated railhead segment, and the thermal expansion it produces enters the mechanical solution directly. In Case 3 the coupled-field formulation is retained so that the element technology is identical to that of Case 4, but no thermal load is applied and the temperature field remains uniform at the reference temperature, so that the response is purely mechanical. No separate thermal analysis is therefore performed in any of the four cases: the temperature is an imposed boundary condition throughout, and is not a quantity predicted from the frictional heat generation of Equation (4), consistent with the treatment described in Section 2.3.

Automatic time stepping is used, and the default ANSYS convergence criteria are retained, namely a force convergence tolerance of 0.5% and a displacement convergence tolerance of 5% of the corresponding reference values. All analyses are quasi-static: the mechanical response is solved in ANSYS Static Structural, in which inertial terms are not included, so that the analysis time (0.2 s for rolling and 0.25 s for full slip) acts as a load-stepping parameter controlling the prescribed motion rather than as a dynamic time coordinate. Neglecting inertia is appropriate here because the contact-zone stress state is governed by the quasi-static contact solution: inertial effects become significant in impact-type wheel–rail problems such as wheel flats, corrugation and turnout crossings, none of which occurs in the smooth constant-speed rolling and stationary wheel spin considered in this study.

The influence of this surface boundary on the computed response is very small. The convective heat loss from the railhead at the maximum imposed temperature rise is of the order of 10^4 W·m^{-2}, whereas the interfacial frictional heat flux estimated in Section 2.3 is of the order of 10^8 W·m^{-2}, a difference of four orders of magnitude. Over the analysis times considered (0.2–0.25 s), the near-surface thermal response is governed by conduction into the bulk rather than by surface losses, and the computed stresses are consequently insensitive to the value adopted for the surface heat-transfer coefficient.

3.6. Loads and Boundary Conditions

The rail base is fully constrained to represent the support provided by the fastenings, sleepers, and foundation. An equivalent vertical load of 80 kN is applied at the axle-hole region of the wheel to simulate the single-wheel load of a Type B metro vehicle; in the full-slip cases an additional small vertical displacement of 0.02 mm is applied to eliminate the initial gap and establish stable initial contact. In the rolling cases, controlled pure rolling is realised by simultaneously imposing longitudinal translation along the

rail and rotation about the axle through a remote displacement: with a running speed of v = 80 km/h (22.22 m/s) and an analysis time of 0.2 s, the wheel translates 4444.4 mm; with a rolling radius of r = 420 mm (wheel diameter of 840 mm), the corresponding pure-rolling rotation is 10.582 rad (606.3°), so that $s \approx 0$. The full-slip cases mainly impose a rotational displacement over an analysis time of 0.25 s, keeping the interface continuously in full sliding. In the coupled rolling case, the railhead temperature boundary rises linearly from 22 °C to 50 °C within 0.2 s; in the coupled full-slip case, it rises from 22 °C to 50 °C within 0.05 s and is then held constant. The two coupled cases share the same moderate thermal boundary for two reasons: first, rolling and full slip are thereby compared at the same heat-input level, which separates the contributions of the motion state and the thermal effect; second, the material parameters in Table 1 are room-temperature values and are valid only within a moderate temperature-rise range. At temperature rises of several hundred degrees the elastic modulus and yield strength decrease markedly and a temperature-dependent constitutive model would be required, which is beyond the assumptions of the present model. The influence of extreme sliding temperature rises is discussed by the analytical extrapolation in Section 4.3.

The thermal load is applied to a fixed region of the railhead rather than to a region that migrates with the contact patch. This represents a locally pre-heated section of rail over which the wheel passes, a condition that arises in service from heat retained after a preceding braking or traction event, or from solar heating of the railhead. This choice is consistent with the interpretation set out in Section 2.3, in which the thermal boundary is treated as an externally imposed thermal load rather than as self-generated frictional heating: the analysis quantifies how a given railhead thermal state modifies the contact response under two different motion states, rather than predicting the temperature that each motion state would itself generate.

The magnitude of the vertical wheel load is set as follows. Type B metro vehicles have a maximum permissible axle load of 14 t, corresponding to a static wheel load of 68.6 kN; the value of 80 kN adopted here therefore includes an allowance of approximately 17% for dynamic wheel-load augmentation under normal running conditions. A single representative load level is used throughout, so that the four cases differ only in the motion state and the thermal boundary. The sensitivity of the results to the wheel load is not investigated in the present study and is noted as a limitation in Section 5.

3.7. Simulation Cases

Four typical cases are set up, as listed in Table 4. Cases 1 and 2 examine the difference in contact response with and without thermal effects in normal rolling; Cases 3 and 4 examine the mechanical and thermo-mechanically coupled responses in full slip.

Table 4. Simulation cases.

Case	Motion State	Analysis Type	Thermal Boundary	Physical Meaning
Case 1	Rolling	Static structural	No	Mechanical contact response in normal rolling
Case 2	Rolling	Thermo-mechanically coupled	Yes	Rolling contact response under moderate heat input
Case 3	Full slip	Static structural	No	Mechanical contact response in full sliding
Case 4	Full slip	Thermo-mechanically coupled	Yes	Coupled response under combined full sliding and thermal effects

The four cases constitute a complete 2 × 2 factorial design, and the conditions under which the two factors may legitimately be regarded as independently varied should be

made explicit. Two model variants are used: a long rail on which the contact patch migrates, required by the rolling motion state, and a short rail on which the patch is stationary, required by the full-slip motion state. The two variants differ in rail length, in the analysis time over which the prescribed motion is applied, and in the duration of the thermal ramp. None of these differences varies with the thermal factor.

The rail length differs only in the extent of rail remote from the contact patch. Both variants use the same CHN60 cross-section, the same railhead crown radius, the same 1.0 mm contact-zone mesh and the same fully constrained rail base, so that the near field of the contact solution is identical; by Saint-Venant's principle the contact response is governed by that near field. The computed results confirm this: the peak contact pressure differs by only 1.9% between Case 1 and Case 3 and the effective contact patch area by about 2%, so that the two variants reproduce essentially the same normal contact solution, and both agree with the Hertz solution to within 3% (Section 3.3).

The difference in analysis time does not correspond to a difference in the physical duration of loading, because all analyses are quasi-static: as stated in Section 3.5, the analysis time is a load-stepping parameter that controls the prescribed motion and does not enter the solution as a dynamic time coordinate. The responses compared in Section 4 are taken from the plateau that each case reaches after its initial transient (see Section 4.1), not from a common instance of time. Likewise, although the thermal ramp durations differ (0.2 s in Case 2 and 0.05 s in Case 4), the two coupled cases are compared in the state after the ramp is completed, in which the railhead is at 50 °C, which is the same in both. The level of the thermal factor is therefore identical at both levels of the motion-state factor, which is what the factorial design requires; it is not required that the two motion-state models be geometrically identical.

The design is balanced in the sense that matters for the analysis of Section 4.4: the thermal factor is realised in exactly the same way at both motion states, and the motion-state factor is realised in exactly the same way at both thermal levels. Any residual difference between the two model variants therefore appears identically in both columns of the design and cancels exactly in the main effect of the thermal factor and in the interaction term. It could in principle bias the main effect of the motion state; that bias is bounded by the agreement between the normal contact solutions of the two variants below 2%, which is small compared with the 14–15% motion-state effect on the rail equivalent stress. The factorial decomposition reported in Section 4.4 is therefore admissible, subject to the restriction—stated there and in the conclusions—that only two levels of each factor are available.

4. Results and Discussion

For a clear comparison of the four cases, this section is organised by physical quantity: the interfacial mechanical characteristics of the contact pressure and friction stress are analysed first, followed by the rail equivalent stress distribution, the thermo-mechanical coupling effects, and a comprehensive comparison.

4.1. Contact Pressure and Friction Stress

Under the 80 kN vertical load, a small, highly stressed local contact patch forms at the wheel–rail interface. The peak contact pressures of the four cases lie in the range of 1.07–1.21 GPa (about 1088 MPa in Case 1, 1209 MPa in Case 2, 1067 MPa in Case 3, and 1194 MPa in Case 4), consistent with the Hertz theory for the same wheel load and with published wheel–rail finite element results [5,9,12]. The contact pressure decays rapidly from the patch centre outward in a typical ellipsoidal spatial distribution, as shown

in Figure 3; in the coupled cases the peak pressure is about 11–12% higher than in the corresponding uncoupled cases owing to thermal expansion of the contact zone.

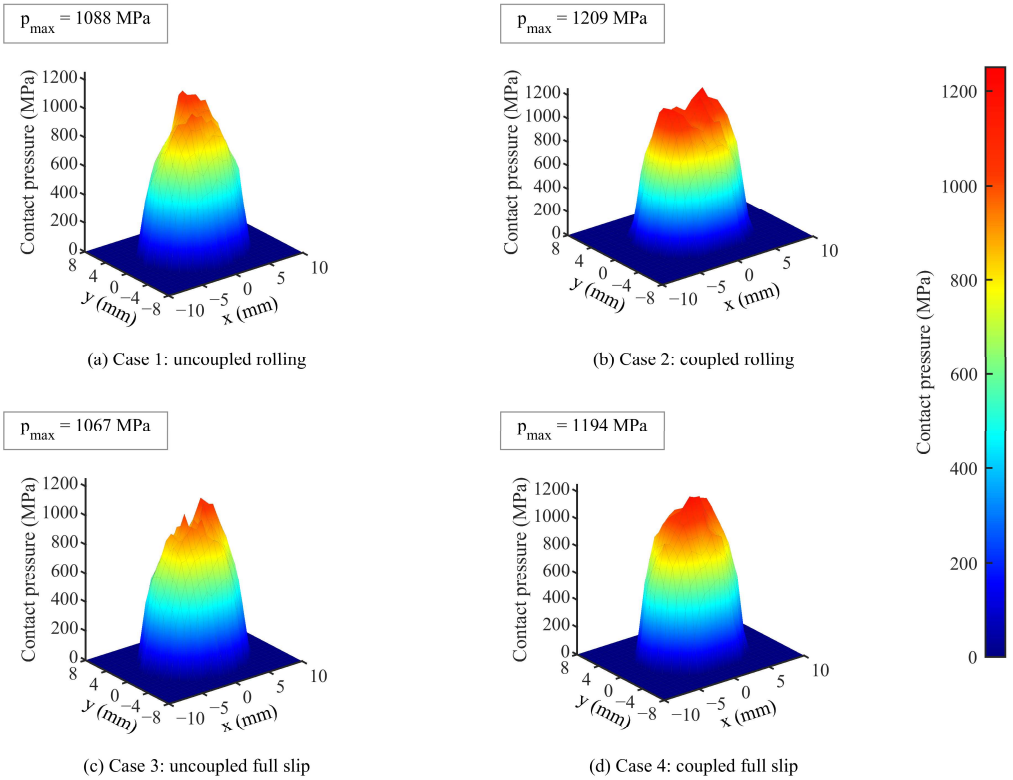


Figure 3. Spatial distributions of the wheel–rail contact pressure in the four cases: (**a**) Case 1, uncoupled rolling; (**b**) Case 2, thermo-mechanically coupled rolling; (**c**) Case 3, uncoupled full slip; (**d**) Case 4, thermo-mechanically coupled full slip. The fields are taken at the final substep of each case and are plotted on a common colour scale of 0–1250 MPa, so that the four panels can be compared directly; the peak contact pressure of each case is annotated above the corresponding panel.

Figure 4 compares the time histories of the interfacial friction stress in the four cases. The friction stress closely follows the contact pressure, with peak-to-peak ratios of 0.26–0.30: in the rolling cases (Cases 1 and 2) no net tangential force is transmitted across the interface (Section 4.2), and this peak-to-peak ratio is about 0.26–0.28, below the friction coefficient of 0.3; in the full-slip cases (Cases 3 and 4) the interface is in full sliding and the ratio reaches about 0.29–0.30, approaching $\mu = 0.3$, in agreement with the Coulomb friction law. The peak friction stresses of the four cases are approximately 294, 334, 320, and 356 MPa, with the highest value in coupled full slip. In the rolling cases the friction stress fluctuates slightly as the contact patch migrates along the rail; in the full-slip cases the contact position is fixed and the curves also show small periodic fluctuations—similar amplitudes with different causes, reflecting the different interfacial characteristics of moving and stationary contact.

The interpretation of this ratio requires care, because its numerator and its denominator are not generally attained at the same material point. It is defined here as the ratio of the peak interfacial friction stress to the peak contact pressure, both taken at the same instant, and it is used solely as an indicator of whether the interface is in partial slip or in full sliding. It is not a traction coefficient, and it is not the abscissa of the shakedown map; that quantity is the global traction coefficient defined in Section 4.2 as the ratio of the tangential to the normal force resultant over the whole patch.

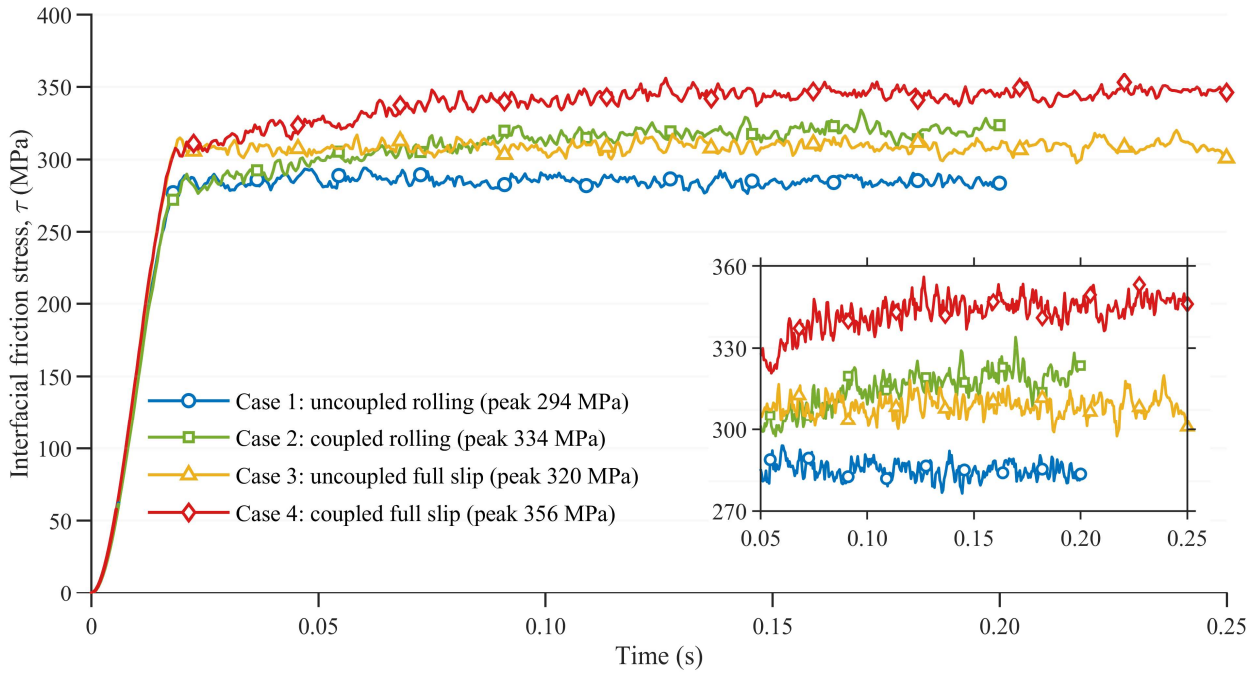


Figure 4. Comparison of the interfacial friction stress time histories in the four cases. The rolling cases end at 0.20 s and the full-slip cases at 0.25 s; the peak value of each case is given in the legend. The inset magnifies the steady-state plateau between 0.05 and 0.25 s, over which the four cases are separated by the thermal and motion-state effects.

The behaviour of the two motion states follows directly from this definition, but it does so for different reasons in the two cases. In the full-slip cases the entire patch slides, so the Coulomb condition $\tau = \mu p n$ holds pointwise and therefore also at the maximum pressure; the two peaks coincide in space and in time; the ratio must equal μ, and the computed values of 0.29–0.30 against $\mu = 0.3$ constitute a consistency check on the tangential contact algorithm rather than an independent result. In the rolling cases the ratio has to be read together with the tangential force resultant reported in Section 4.2, which is 0.12 kN. Distributed over the finite element contact area of 154.3 mm^2, that resultant corresponds to an area-averaged longitudinal traction of 0.78 MPa, smaller than the peak local traction magnitude of 294 MPa by a factor of about 380. The tangential traction field in rolling is therefore not unidirectional: its local magnitude reaches 0.90 of the Coulomb limit evaluated at the peak pressure, but the traction vectors do not share a common direction and very nearly cancel upon integration over the patch. This is the self-equilibrating traction field characteristic of free rolling, in which neither a traction nor a braking torque is applied [44]; in the present geometry the departure of the local traction directions from the rolling direction is attributable to the spin component of the creepage, which does not vanish because the contact normal is inclined by the combination of the LM tread profile, the railhead crown radius and the 1:40 rail cant [28]. The computed values of 0.26–0.28 are accordingly a measure of the local traction magnitude alone. They carry no information about the tangential force transmitted across the interface, and the two must not be conflated—which is exactly the distinction drawn above between this local indicator and the global traction coefficient of Section 4.2.

The contact patch itself deserves further attention. The normal load is 80 kN in all four cases, and the integral of the contact pressure over the patch must balance it; approximating the pressure as a Hertzian ellipsoidal distribution (mean pressure of about two-thirds of the peak), the effective patch areas of the four cases are estimated at about 110, 99, 112, and 100 mm^2. The patch is thus not invariant: in the coupled cases, the thermal

expansion of the heated railhead bulges the crown outward and concentrates the contact, shrinking the effective area by about 10% relative to the corresponding uncoupled cases, which corresponds to the 11–12% increase in peak pressure and satisfies load conservation. The patch areas in rolling and full slip are close to each other, and the difference between the two motion states lies mainly in the interfacial tangential state rather than in the patch geometry—a self-equilibrating traction field transmitting almost no net force in rolling versus full sliding over the entire patch in full slip.

Two measures of the contact patch area are reported here, because they quantify different things and are not interchangeable. The effective area A_eff quoted above follows from load conservation under an assumed Hertzian pressure distribution. Therefore, it weights the patch by the pressure it actually carries; it is the quantity that enters the load balance directly, which is why it was adopted in the first place. The finite element contact area A_FE is extracted from the solution itself, as the summed area of the interface elements whose contact status is sticking or sliding; it consequently includes the peripheral elements that transmit only a very small pressure, and its boundary is quantized by the element size. Both are listed in Table 5, together with the Hertz elastic reference of 102.3 mm^2 obtained for the same geometry and load in Section 3.3.

Table 5. Contact patch area of the four cases evaluated by two independent measures. A_FE is extracted directly from the finite element contact status; A_eff is inferred from the peak contact pressure under a Hertzian distribution assumption. The Hertz elastic reference for the same geometry and load is 102.3 mm^2 (Section 3.3).

Case	A_FE (mm^2)	A_eff (mm^2)	A_FE/A_eff
Case 1: rolling	154.3	110.3	1.40
Case 2: rolling, coupled	141.3	99.3	1.42
Case 3: full slip	157.7	112.5	1.40
Case 4: full slip, coupled	139.9	100.5	1.39

The FE contact area exceeds the pressure-inferred effective area by a factor of 1.39 to 1.42 in all four cases. A comparable ratio follows from the independent elastic–plastic analysis of Kim and Kim [41], whose contact patch semi-axes of 7.50 mm × 6.30 mm exceed their Hertz values of 6.54 mm × 5.18 mm by 39% in area. More important than the absolute values, however, is that the two measures agree on every comparison from which the conclusions of this study are drawn. The thermal boundary reduces the patch by 8.4% and 11.3% under the two motion states when measured by A_FE, and by 10.0% and 10.7% when measured by A_eff. The change in motion state alters the patch by +2.2% and −1.0% under the two thermal states when measured by A_FE, and by +2.0% and +1.2% when measured by A_eff; the sign is not even consistent, which confirms that the normal contact response is almost insensitive to the motion state. The conclusions of Sections 4.4 and 5 therefore do not depend on which convention is adopted.

In Figure 4, the friction stress of each case enters a relatively steady plateau after the initial transient. In rolling, the patch continuously moves onto fresh rail surface of identical nominal geometry, so the contact response reaches a quasi-steady state after the initial loading and plastic conforming are completed, and the small periodic fluctuations stem mainly from the patch boundary crossing discrete mesh elements; in full slip, the material at the fixed patch undergoes local plastic conforming with a slight patch growth in the early loading stage and then shakes down under bilinear hardening, with the patch geometry stabilising; in the coupled cases, a slowly rising trend is superimposed during the temperature ramp (0–0.2 s in Case 2 and 0–0.05 s in Case 4), corresponding to the heat-induced contact concentration process. The plateau therefore reflects the patch geometry

stabilising after its initial evolution rather than an unchanging patch; over the whole process the patch-area variation is on the order of 10% (Figure 5), and the stress time histories fluctuate mildly about stable values.

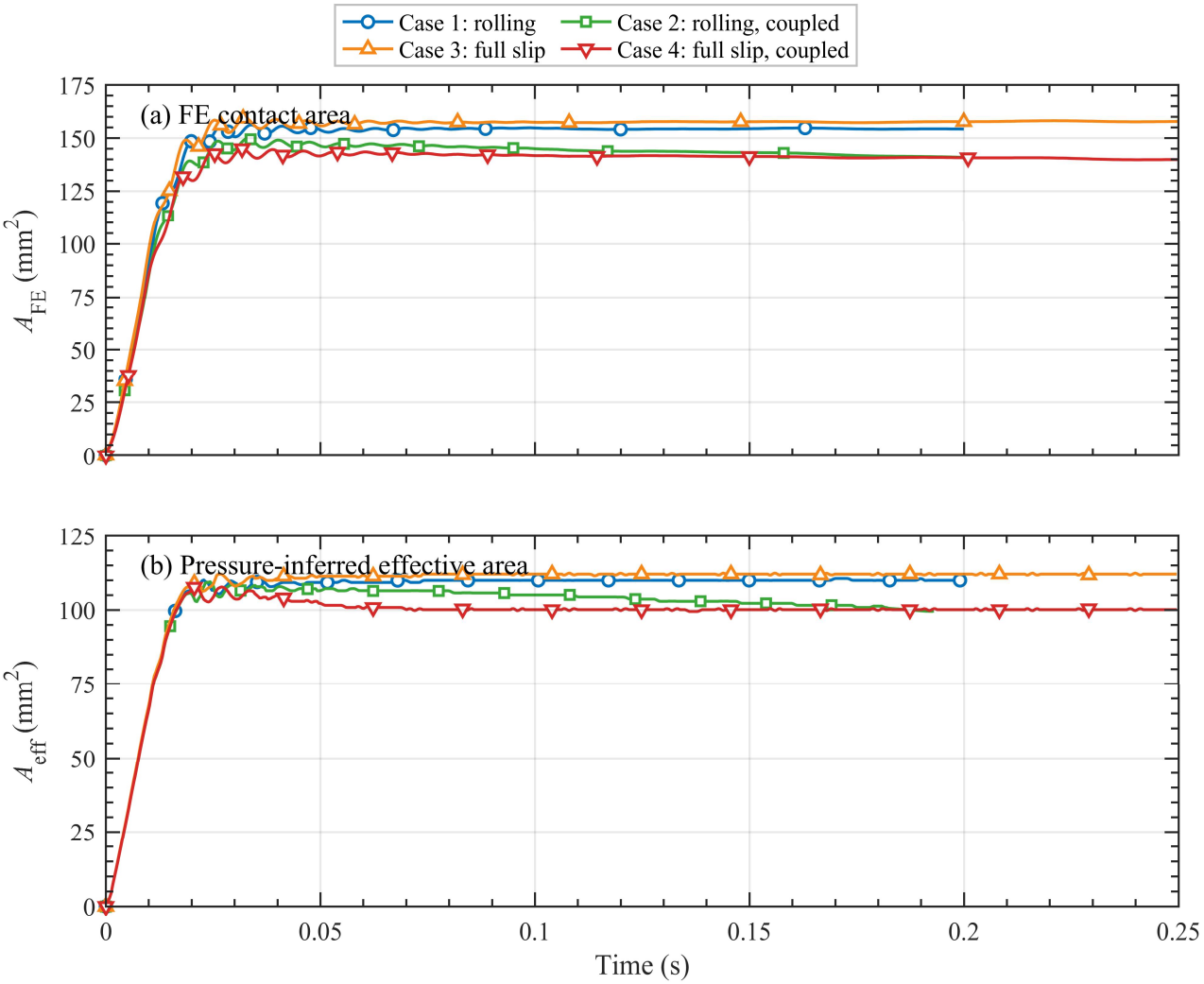


Figure 5. Contact patch area versus time in the four cases: (**a**) the FE contact area A_FE, extracted from the contact status of the interface elements; (**b**) the pressure-inferred effective area A_eff. The legend applies to both panels.

4.2. Rail Equivalent Stress

Figure 6 shows the rail equivalent stress distributions of the four cases. In the two uncoupled cases (Cases 1 and 3) the high-stress zone is confined to the immediate neighbourhood of the contact patch on the railhead and decays rapidly toward the rail web, exhibiting the transfer characteristics of a purely local contact stress field. In the two coupled cases (Cases 2 and 4) a second, spatially extended stress field is superimposed upon it: the whole heated railhead segment carries an elevated stress level over its entire length, and the local contact concentration is embedded within it. The maximum rail equivalent stresses of the four cases are 541.9, 596.3, 623.1, and 679.5 MPa, respectively.

Notably, all four maxima reach and exceed the 457 MPa yield strength of U71Mn rail steel, indicating that under the 80 kN wheel load the contact patch has entered a shallow-layer plastic state while the bulk material around the patch remains elastic. This is consistent with the repeated local yielding and progressive shakedown experienced by the contact zone in wheel–rail rolling contact fatigue [14,45,46]. The comparison shows that, for the same motion state, the coupled cases exhibit higher rail equivalent stress than the

uncoupled ones (Case 2 exceeds Case 1 by about 10.1%, and Case 4 exceeds Case 3 by about 9.0%) owing to the additional thermal stress at the moderate temperature rise; for the same thermal boundary, the full-slip cases are higher than the rolling ones (Case 3 exceeds Case 1 by about 15.0%, and Case 4 exceeds Case 2 by about 14.0%) because the interface enters full sliding and the complete tangential traction raises the surface-layer equivalent stress. Combining both factors, coupled full slip (Case 4) has the highest rail equivalent stress.

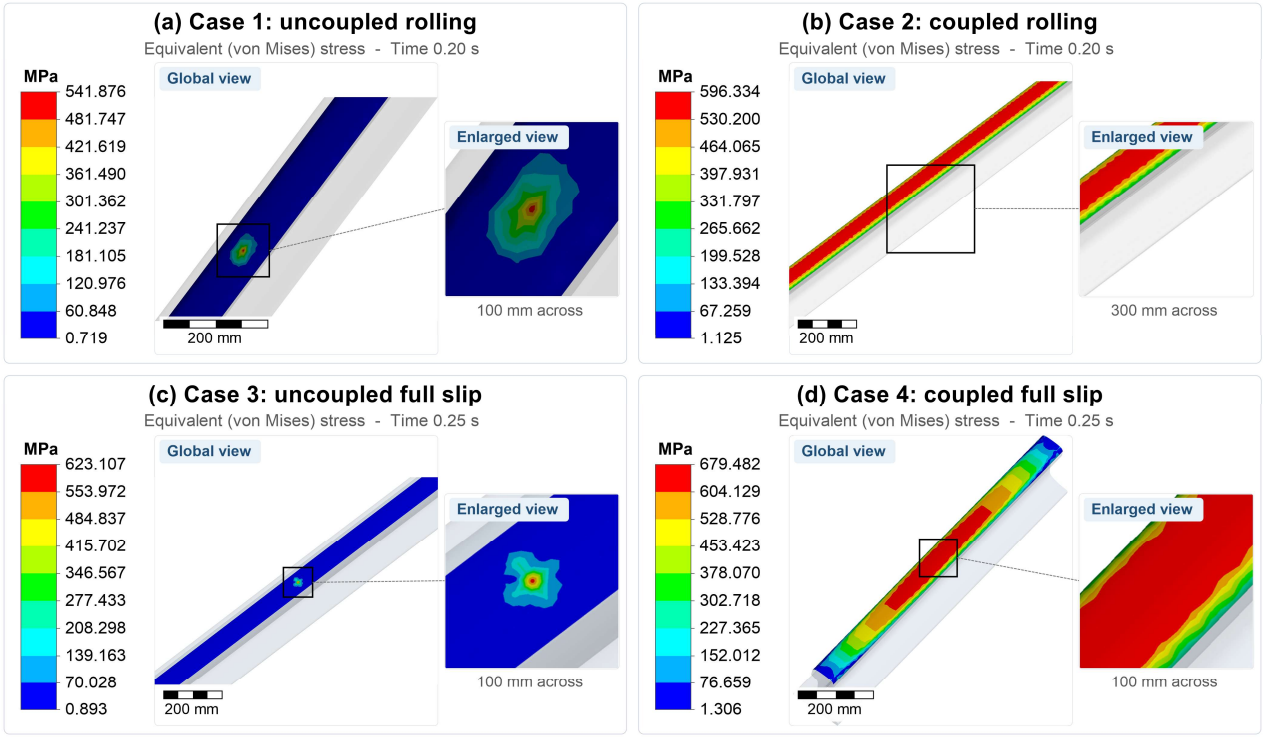


Figure 6. Distributions of the rail equivalent (von Mises) stress in the four cases: (**a**) Case 1, uncoupled rolling; (**b**) Case 2, thermo-mechanically coupled rolling; (**c**) Case 3, uncoupled full slip; (**d**) Case 4, thermo-mechanically coupled full slip. Each panel is reproduced with the colour scale of its own solution as exported from the post-processor, and the band boundaries are listed in the legend beside it; the colours are therefore not directly comparable between panels, and the comparison between the cases is made on the values, which are summarised in Table 6. Each panel pairs a global view of the rail with an enlarged view of the railhead region outlined by the box, which resolves the stress localization within and around the contact patch. The enlarged views cover a 100 mm wide field of view, except in (**b**), where 300 mm is used because in that case the elevated stress extends along the whole heated railhead segment instead of concentrating at the contact patch. The scale bar is 200 mm in every panel.

Table 6. Summary of the main simulation results of the four cases.

Case	Motion State	Thermal Boundary	Peak Contact Pressure (MPa)	Peak Friction Stress (MPa)	Max. Rail Equivalent Stress (MPa)	Max. Equiv. Plastic Strain (%)	Remark
Case 1	Rolling	No	≈1088	≈294	541.9	2.1	Reference; shallow plasticity in the patch
Case 2	Rolling	Yes	≈1209	≈334	596.3	3.3	Additional thermal stress; +10.1% vs. Case 1
Case 3	Full slip	No	≈1067	≈320	623.1	4.0	Full sliding; +15.0% vs. Case 1
Case 4	Full slip	Yes	≈1194	≈356	679.5	5.2	Most unfavourable; highest friction energy

The two spatial patterns just described correspond to two distinct mechanisms, and it is useful to keep them apart. Both originate in the same constrained thermal expansion, but they act at different length scales. The heated railhead segment is restrained longitudinally by the fully fixed rail base and by the surrounding unheated rail, so that it cannot expand freely along the rail; the restrained in-plane expansion generates a compressive thermal stress distributed over the whole heated length, and this volumetric mechanism is what raises the stress level along the entire railhead in Figure 6b,d. Expansion in the direction normal to the running surface is by contrast unrestrained, so the heated crown bulges slightly outward, which sharpens the effective local curvature at the interface and concentrates the contact; this local mechanism is the one responsible for the 11–12% increase in peak contact pressure and the 8–11% reduction in contact patch area reported in Section 4.1.

This distinction also identifies the part of the thermal response which is sensitive to the idealisation of the rail base. The volumetric contribution scales with the degree of longitudinal constraint and would be reduced by a more compliant fastener-and-ballast support, so that the fully fixed base adopted here renders it a conservative upper estimate, as already noted in Section 4.3. The local contribution is set by the thermal expansion of the material within a few millimetres of the interface and is essentially insensitive to the support condition. The interfacial quantities of Section 4.1—peak contact pressure, friction stress and contact patch area—are accordingly the more robust of the two with respect to this modelling choice, and the equivalent-stress increment should be read as an upper bound.

To further identify the nature of the plastic response in the contact zone, the four cases are positioned in the shakedown map [39,47]. With the shear yield strength of U71Mn taken as $k = 457/\sqrt{3} \approx 264$ MPa, the normalised contact pressures p_0/k of the four cases are about 4.1, 4.6, 4.0, and 4.5, where the thermally concentrated peak pressures are used for the coupled cases so that their positioning errs on the conservative side. Two indicators must be distinguished in the positioning: the abscissa of the shakedown map is the global traction coefficient f (the ratio of the tangential force resultant to the normal force resultant), whereas the peak-to-peak friction-to-pressure ratio of Section 4.1 (0.26–0.30) is a local interfacial indicator and cannot be used directly as f. In the rolling cases the two differ by more than two orders of magnitude, because the local tractions are large in magnitude but self-equilibrating and therefore transmit almost no net force (Section 4.1). The rolling cases (Cases 1 and 2) are controlled pure rolling without applied traction or braking torque; the assumption $f \approx 0$ is not made a priori here but verified directly against the finite element solution: the longitudinal tangential force resultant extracted from the contact solution is 0.12 kN against a normal load of 80 kN, that is, $f = 1.5 \times 10^{-3}$. The margin on this value is wide, because the surface branch of the shakedown limit falls below the subsurface branch only above $f = 1/4.68 = 0.214$, which corresponds to a tangential resultant of 17.1 kN; the computed resultant is smaller than that by a factor of about 140, so the positioning of the rolling cases under the subsurface criterion is insensitive to its precise value. Accordingly $f \approx 0$ and the subsurface criterion governs—under pure rolling the elastic shakedown limit of three-dimensional point contact is about $p_0/k \approx 4.7$ [39]: Case 1 (4.1) lies within the elastic shakedown boundary, consistent with the time histories in Section 4.1 that settle down after first-pass local yielding, while Case 2 (4.6) approaches this limit under the additional thermal stress. In the full-slip cases (Cases 3 and 4) the interface enters full sliding and the global traction coefficient equals the friction coefficient, $f = 0.3$, so the governing criterion switches to the surface shakedown boundary $1/f \approx 3.3$ [39,47]: both cases (4.0 and 4.5) clearly exceed it and fall in the surface ratchetting (incremental plastic flow) regime, implying that the rail surface layer will accumulate plastic deformation under

repeated loading, in agreement with field observations of rail burns and surface-initiated rolling contact fatigue.

Full slip thus worsens the rail service state through two routes: it switches the governing criterion from the subsurface shakedown limit (≈4.7) to the stricter surface ratchetting boundary (≈3.3), and it pushes the operating point from inside the shakedown boundary into the ratchetting regime. Moreover, the tangential traction level determines the depth of the highly stressed zone: at low traction the maximum shear stress lies in the subsurface at a depth of about 0.48*a* (*a* being the contact patch radius) below the patch centre, and as the traction coefficient increases toward 0.3 the onset of yielding migrates to the surface [39]. This is precisely the origin of the equivalent-stress increment in full slip—its normal contact solution is essentially the same as in rolling (the peak contact pressure is even slightly lower), and the increment comes mainly from the complete tangential traction pulling the high-stress zone toward the surface.

The computed plastic strain confirms this mechanism directly. The maximum equivalent plastic strain of the four cases is 2.1%, 3.3%, 4.0% and 5.2% respectively, and its position differs sharply between the two motion states. In uncoupled rolling the maximum lies 2.1 mm below the running surface; in uncoupled full slip it lies at 0.3 mm, that is, within the first element layer beneath the running surface and effectively at the surface itself. The contrast between the two locations is thus resolved by the present mesh, whereas the precise depth in full slip, being smaller than the 1.0 mm contact-zone element size, is not. The subsurface depth found in rolling is of the same order as the classical elastic estimate of 0.48a ≈ 3.1 mm and somewhat shallower than it, as is to be expected once the redistribution of stress by plastic flow is taken into account. The two positions correspond to the two global traction coefficients established above, f = 1.5×10^{-3} in rolling and f = 0.3 in full slip. The migration of the onset of yielding from the subsurface towards the surface as the traction coefficient approaches 0.3, which the shakedown argument invokes as the reason for the change in governing criterion, is therefore not assumed here but obtained from the simulations.

The computed plastic strains are also consistent with the constitutive law itself. For bilinear isotropic hardening the equivalent stress and the equivalent plastic strain are related by σe = σs + Hεp, with the plastic modulus H = EEt/(E − Et) formed from the parameters of Section 3.2. Applied to the four computed plastic strains, this relation reproduces the four computed maxima of the rail equivalent stress to within 1.5%. This constitutes an independent check on the elastic–plastic part of the solution, complementary to the contact-mechanics verification of Section 3.4.

The positioning of the four cases is shown graphically in Figure 7, in which the classical shakedown map for three-dimensional point contact is reproduced with the subsurface elastic shakedown limit of $p_0/k = 4.68$ at low traction and the surface flow limit of $p_0/k = 1/f$ at high traction; above f ≈ 0.30 the two limit curves coincide, because a protective residual stress field cannot develop against surface shear. The figure makes the mechanism plain: the two rolling cases and the two full-slip cases are hardly separated at all in ordinate—4.1 against 4.0 without the thermal load, and 4.6 against 4.5 with it—and are separated instead by the boundary that governs them at their respective abscissae. It is the change in governing criterion, not a change in contact pressure, that moves the full-slip cases across the boundary.

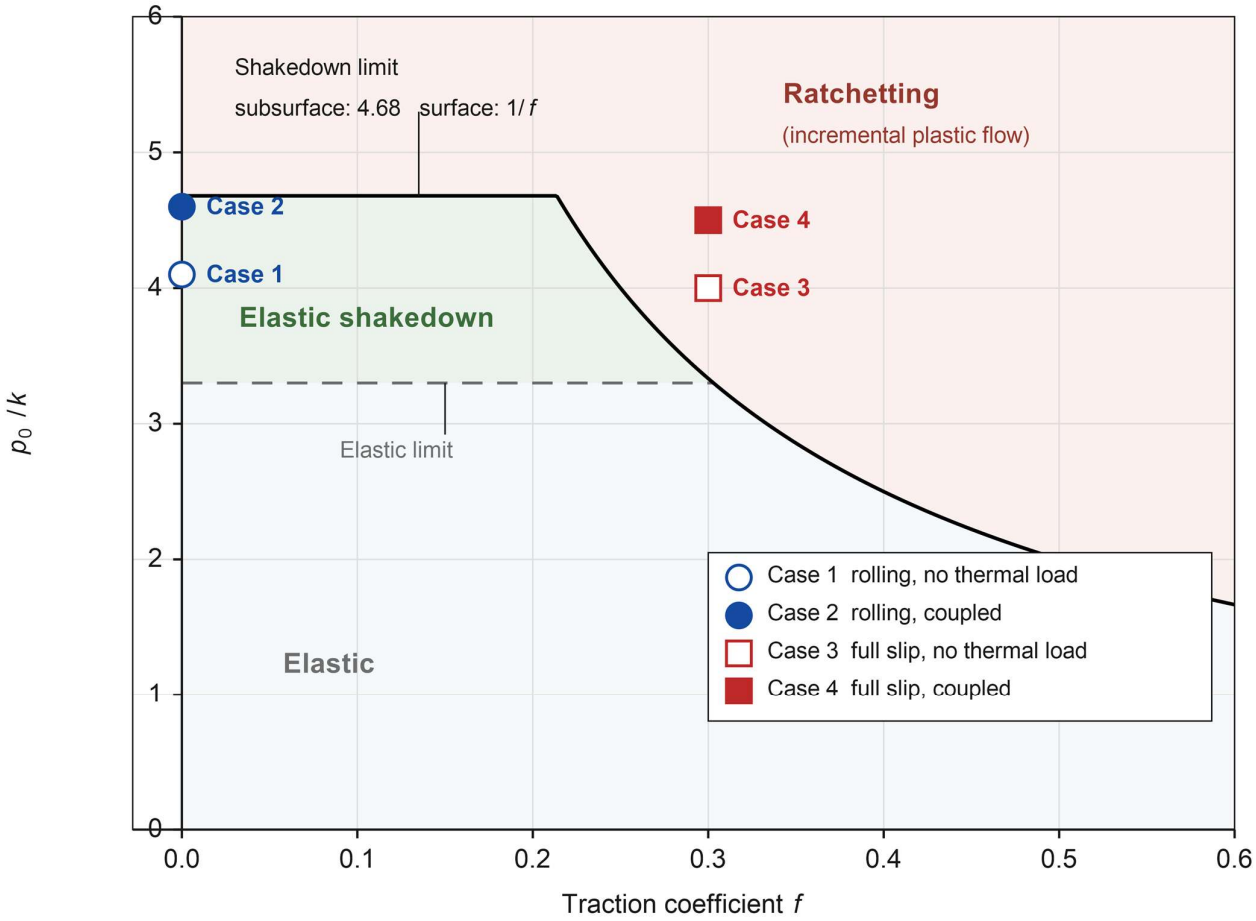


Figure 7. Positioning of the four cases on the classical shakedown map for three-dimensional point contact. Solid curve: shakedown limit, with the subsurface branch of $p_0/k = 4.68$ and the surface branch of $p_0/k = 1/f$. Dashed curve: elastic limit, with the subsurface branch of $p_0/k = 3.30$. Circles denote the rolling cases, at a global traction coefficient of $f \approx 0$; squares denote the full-slip cases, at $f = 0.3$. Open symbols are the uncoupled cases and filled symbols the thermo-mechanically coupled ones, for which the thermally concentrated peak contact pressures are used. The shear yield strength of U71Mn is taken as $k = 457/\sqrt{3} \approx 264$ MPa. The map shows the positioning for the single loading pass analysed here and identifies the operating regime; it is not a quantitative measure of the cyclic ratchetting rate, which requires multi-pass analysis.

The applicability of the classical shakedown map to the present model requires comment. The shakedown boundaries were derived for an elastic–perfectly plastic material subjected to a Hertzian pressure distribution without thermal stress, whereas the present simulations involve bilinear isotropic hardening, an imposed thermal load, and a non-Hertzian contact pressure distribution modified by local yielding. The map is therefore used here as a qualitative positioning tool rather than as a quantitative failure criterion. Recent finite element reconstructions of the wheel–rail shakedown map indicate that the classical boundaries are conservative, with the reconstructed three-dimensional shakedown surfaces of hardening materials lying consistently above them [48]; the elastic shakedown limit of a nonlinear kinematic hardening material falls between those of an elastic–perfectly plastic material and a linear kinematic hardening material. The positioning reported above is accordingly a conservative indication. The hardening rate adopted here is in any case modest, where $E_t/E \approx 1/49$, so that the constitutive response lies close to the elastic–perfectly plastic idealisation for which the classical boundaries were derived, and the correction associated with hardening is correspondingly small.

A further qualification concerns the thermal load. The boundaries plotted in Figure 7 are isothermal, having been derived for mechanical contact loading alone. Böhmer et al. [49] computed the shakedown limit of rail surfaces with material hardening and thermal stresses both included, and found that the thermal stresses at the rail surface reduce the elastic limit, so that yielding begins at lower mechanical loads, and reduce the shakedown limit as well; the analytical treatment of thermal stresses in wheel–rail contact by Ertz and Knothe [50] leads to the same conclusion. Two corrections therefore act on the plotted boundary for the coupled cases, and they act in opposite senses: hardening raises it, as noted above, whereas the thermal stress lowers it. Their net effect is not determined by the present analysis, which is a further reason for reading Figure 7 as a qualitative positioning rather than as a quantitative margin against failure. For the two uncoupled cases only the first correction applies, and their positioning is unambiguously conservative.

Two further limitations follow. First, ratchetting is by definition associated with repeated loading and the progressive accumulation of plastic strain, whereas the present analysis considers a single loading pass. The results therefore indicate an increased tendency towards surface plastic flow; they do not by themselves demonstrate the occurrence of ratchetting, the formation of rail burns, or the initiation of rolling contact fatigue, all of which would require cyclic, multi-pass simulation. Second, the isotropic hardening model adopted here cannot represent the Bauschinger effect or progressive plastic accumulation under cyclic loading; a kinematic or combined hardening description would be required for that purpose. Cyclic analysis with such a constitutive model is identified as the natural continuation of this work. The position of the two full-slip cases within the ratchetting region of Figure 7 is accordingly a single-pass indication that the rail surface layer lies above the shakedown limit, and not a quantitative prediction of the plastic strain that would accumulate per loading cycle, which only cyclic, multi-pass analysis with such a hardening model can provide.

4.3. Thermo-Mechanical Coupling Effects

In the coupled cases, the railhead temperature boundary rises from 22 °C to 50 °C ($\Delta T \approx 28$ °C). By Equation (8), the free thermal strain of the railhead is about $\alpha \Delta T = 1.10 \times 10^{-5} \times 28 \approx 3.1 \times 10^{-4}$. Constrained by the surrounding material and the substructure, this expansion produces additional thermal stress which, when superimposed on the mechanical contact stress, raises the rail equivalent stress of the coupled cases by about 9–10% relative to the uncoupled ones. Regarding frictional energy, the coupled full-slip case accumulates about 5000 J of interfacial friction work within 0.25 s (an average power of about 20 kW) because the interface slides continuously; in rolling, the physical friction work arises only from the local micro-slip at the patch edge and is far smaller than in full sliding—this difference in frictional heat input is the direct reason why full slip is more prone to inducing rail thermal damage. As stated in Section 2.3, the 22–50 °C boundary is an externally imposed moderate thermal load, applied identically to both motion states as a control variable, and does not represent the self-generated contact temperature. The imposed rise is therefore best read as representing a railhead that is already moderately warm when the wheel reaches it—for instance from solar heating, or from heat retained after an earlier braking or traction event—and it provides a conservative lower-bound reference for such pre-heated or warm-ambient railheads rather than a representation of the several-hundred-degree flash temperatures of an actual sliding burn, which lies outside the validity of the room-temperature material model of Table 1 and is treated only through the analytical bound of Section 2.3. The analytical estimate of Section 2.3 indicates that continuous full sliding would produce railhead temperature rises in the order of 10^3 °C, that is, two orders of magnitude above the imposed value; this is consistent with the

several-hundred-degree contact temperatures reported experimentally and numerically in the literature [7,8,18,19,42]. The martensitic white etching layer characteristic of rail burns requires contact temperatures above the austenitizing temperature of about 727 °C followed by rapid cooling [13,34].

Two consequences follow. First, the thermal contribution of about 9–10% obtained here is a conservative lower bound for the full-slip cases, because the real thermal loading in continuous sliding is far more severe than that imposed. Second, the room-temperature material parameters of Table 1 are valid only over a moderate temperature range. Measurements on U71Mn rail steel over 20–800 °C show a marked reduction in flow stress with increasing temperature [38], and at several hundred degrees the elastic modulus, yield strength and thermal properties all change appreciably, while material softening and phase transformation become active. A quantitative extrapolation of the present results to that range is therefore not attempted. Characterising the extreme-sliding regime requires a temperature-dependent constitutive model together with a fully predictive thermal solution, and is left for future work.

Within the moderate range actually simulated, the mechanism of the thermal contribution can be stated quantitatively. The free thermal strain of the railhead at $\Delta T \approx 28$ °C is $\alpha\Delta T \approx 3.1 \times 10^{-4}$ (Equation (8)). Constrained by the surrounding material and by the substructure, this expansion produces additional thermal stress. The computed rail-equivalent-stress increment of 54–56 MPa corresponds to a slope of about 2.0 MPa·°C^{-1}, which is about 85% of the slope obtained under full constraint (the product of the elastic modulus and the expansion coefficient, about 2.3 MPa·°C^{-1}). This ratio provides a quantitative measure of the degree of constraint imposed by the fully fixed rail base: the railhead is strongly, but not completely, constrained. A more compliant support would relieve part of this longitudinal constraint. In a real track the rail is held to the sleepers through resilient rail pads of finite longitudinal and rotational stiffness, and the sleepers themselves can move within the ballast, so that a locally heated segment is free to expand into the cooler adjacent rail and to lift and rotate slightly rather than being held rigidly; only continuously welded rail with a high longitudinal fastening resistance approaches the fully fixed base assumed here. The true longitudinal restraint therefore lies between free expansion and full fixity, so that the thermal-stress slope computed here is an upper estimate that a resilient fastener-and-ballast support would move towards the lower end of that range. The fully constrained idealisation adopted here therefore yields a conservative estimate of the thermal contribution, which is noted as a limitation of the model.

4.4. Comprehensive Comparison of the Four Cases

The main results of the four cases are summarised in Table 6. In uncoupled rolling, the contact response is governed mainly by the mechanical load and the stress level is the lowest; coupled rolling raises the rail equivalent stress slightly through the additional thermal stress; uncoupled full slip concentrates the rail equivalent stress and friction stress because the contact position is fixed and the tangential traction reaches full sliding, and coupled full slip, combining full sliding and temperature rise, exhibits the strongest frictional energy input and local contact response and is the most unfavourable of the four cases.

It is worth noting that the four cases form a full 2×2 factorial combination of motion state $\times$ thermal boundary, from which the degree of coupling between the two factors can be assessed quantitatively. Taking Case 1 (541.9 MPa) as the reference, the thermal-effect increments under the two motion states are 54.4 and 56.4 MPa—essentially equal—and the motion-state increments under the two thermal boundaries are 81.2 and 83.2 MPa—also essentially equal. Linear superposition predicts $541.9 + 54.4 + 81.2 \approx 677.5$ MPa for Case 4,

only 2.0 MPa (0.3%) below the computed value of 679.5 MPa. The interaction term defined by factorial analysis (Case 4 − Case 3 − Case 2 + Case 1) is +2.0 MPa, less than 4% of either main effect. Therefore, within the two thermal states considered, the interaction between the motion-state effect and the thermal effect is weak. This indicates that, for the specific conditions examined, the two effects may to a good approximation be evaluated separately; it does not establish general linear additivity, which would require additional thermal levels. The magnitude of the interaction cannot be assumed a priori and must be determined by computation. The interaction is expected to grow at high temperature rises owing to material softening and stronger thermo-mechanical coupling, and verification over a range of temperature rises is identified as ongoing work.

4.5. Sensitivity and Robustness of the Results

Because the conclusions drawn above rest on differences in the order of ten per cent, the sensitivity of those differences to the principal model parameters requires examination. Five parameters are considered: the friction coefficient, the wheel load, the imposed temperature rise, the thermal contact conductance and the convective heat-transfer coefficient.

The friction coefficient is the parameter to which the tangential response is most directly tied to, and the present study already contains a scan of its effect over the whole admissible range. The global traction coefficient transmitted across the interface is 1.5×10^{-3} in the rolling cases and 0.3 in the full-slip cases (Section 4.2), so that the four cases span the entire interval between a traction-free interface and full tangential saturation at $\mu = 0.3$. Over that interval the normal contact response is essentially unchanged—the peak contact pressure differs by 1.9% and the patch area by about 2%—whereas the maximum rail equivalent stress increases by 15%. The sensitivity of the equivalent stress to the transmitted traction is therefore about 5% per 0.1 of the traction coefficient, so that a variation in μ across the 0.30–0.35 interval measured for U71Mn under dry room-temperature conditions [24,25] would alter the maximum equivalent stress by about 2.5%, and would leave the normal contact quantities unaffected. The positioning on the shakedown map is robust over the same interval: the surface branch $p_0/k = 1/f$ takes the values 4.00, 3.33 and 2.86 for $\mu = 0.25$, 0.30 and 0.35 respectively, all of which lie below the ordinates of the full-slip cases, which therefore remain in the ratchetting regime throughout.

The sensitivity to the wheel load follows from Hertzian scaling, $p_0 \propto W^{(1/3)}$ and $A \propto W^{(2/3)}$, a relation that the present model reproduces to within 2.7% in its elastic limit (Section 3.3). A change of $\pm 12.5\%$ in the wheel load, from 80 kN to 70 or 90 kN, accordingly changes the peak contact pressure by about -4.4% and +4.0% and the contact patch area by about -8.5% and +8.2%. Local yielding reduces the pressure sensitivity below this elastic estimate and increases the area sensitivity above it, since the two errors are locked together by conservation of the applied load, as discussed in Section 3.3. The ordinate of the shakedown map scales with the peak contact pressure, so that a 12.5% change in wheel load displaces the four operating points by about 4% in p_0/k, which does not alter the regime in which any of them falls under.

The sensitivity to the imposed temperature rise is constrained analytically. Within the moderate range considered, the thermal strain is linear in the temperature change, so that the additional thermal stress is proportional to ΔT and is bounded above by $E\alpha\Delta T$; the computed slope of about 2.0 MPa·°C^{-1} is 85% of that bound (Section 4.3). The thermal contribution to the maximum equivalent stress at any temperature rise within the range of validity of the room-temperature material data of Table 1 is therefore bounded between zero and 2.31 MPa·°C^{-1} multiplied by that rise. The two thermal levels examined here do not establish the behaviour beyond that range, and the corresponding limitations are stated in Sections 4.3 and 4.4.

The thermal contact conductance and the convective heat-transfer coefficient do not require a parameter scan, for the reason set out in Section 3.5. Because the railhead temperature is imposed as a temperature degree-of-freedom constraint, the temperature of the heated segment is fixed by that constraint irrespective of the interfacial heat balance, so that neither of the parameter enters the determination of the thermal load that drives the rail stress. To the extent that either does influence the interfacial heat balance, a larger conductance or a larger convection coefficient removes more heat from the railhead and therefore lowers, rather than raises, the thermal stress; overestimating either parameter can accordingly only under-report the thermal effect, never exaggerating it.

Finally, the numerical uncertainty of the comparison is itself smaller than the effects being compared. The discretisation uncertainty of the adopted mesh is below 2.5% (Section 3.3); the residual differences between the two model variants affect only the motion-state main effect and are below 2% (Section 3.7); the two independent measures of the contact patch area agree on every comparison from which the conclusions are drawn (Section 4.1). The differences of 8–15% on which Sections 4.4 and 5 rest on therefore lie well outside the combined uncertainty of the model.

5. Conclusions

A three-dimensional elastic–plastic finite element model of a single wheel and a single rail of a Type B metro vehicle was established, and the contact pressure, friction stress and rail equivalent stress were compared among four cases forming a 2×2 combination of two motion states (pure rolling and full slip) and two thermal states (no thermal load, and a prescribed railhead temperature rise from 22 °C to 50 °C). The temperature field was imposed as a prescribed thermal boundary rather than solved from frictional heating, and the same boundary was applied under both motion states as a control variable, so that the two effects could be separated. The main findings are grouped below according to the level of evidence supporting them.

Results obtained directly from the simulations are summarised below.

(1) Changing the motion state has little influence on the normal contact response: from pure rolling to full slip the peak contact pressure changes by less than 2% and the contact patch area is nearly unchanged. The interface, however, changes from local micro-slip to full sliding; the peak-to-peak friction-to-pressure ratio rises from 0.26 to 0.28 to 0.29–0.30, and the maximum rail equivalent stress increases by about 14–15%. The essential role of the motion state is therefore not to change the normal contact load, but to strengthen the tangential traction and move the high-stress zone towards the rail surface layer. This shift is confirmed directly by the computed plastic strain, whose maximum lies 2.1 mm below the running surface in rolling but at 0.3 mm in full slip.

(2) Under the prescribed 28 °C railhead temperature rise, the contact patch area decreases by about 8–11%, depending on the case and on which of the two measures of Table 5 is adopted. The peak contact pressure increases by about 11–12%, and the maximum rail equivalent stress increases by about 9–10%, through local thermal expansion concentrating the contact. The corresponding thermal-stress slope is about 2.0 MPa·°C^{-1}, or about 85% of the fully constrained theoretical value.

(3) For the two thermal states considered, the interaction term of the 2×2 comparison is +2.0 MPa, less than 4% of either main effect, indicating a weak interaction between the motion-state effect and the thermal effect for the specific conditions examined. The maximum rail equivalent stresses of the four cases are 541.9, 596.3, 623.1 and 679.5 MPa, all exceeding the 457 MPa yield strength of U71Mn rail steel, indicating shallow localised plasticity in the contact patch. The combination of full slip and thermal loading is the most unfavourable of the four cases.

Estimates obtained analytically rather than by simulation are summarised below.

(4) Positioning on the classical shakedown map places the rolling cases, for which the tangential force resultant extracted from the contact solution gives $f = 1.5 \times 10^{-3}$, within or at the edge of the subsurface elastic shakedown limit, and the full-slip cases ($f = 0.3$) beyond the surface ratchetting boundary. Since the classical boundaries are conservative for hardening materials, this single-pass result indicates an increased tendency towards surface plastic flow, rather than demonstrating that ratchetting, rail burns or rolling contact fatigue occurs; quantifying the plastic strain accumulated under repeated passes requires cyclic, multi-pass analysis.

(5) An analytical estimate based on Equation (4) indicates that continuous full sliding would produce railhead temperature rises in the order of 10^3 °C, far above the value imposed here. The thermal contribution reported in (2) is therefore a conservative lower bound, as is the thermal stress computed under the fully constrained rail base.

Scope of validity and outstanding questions are summarised below.

(6) The results above are valid for the particular wheel load (80 kN), friction coefficient ($\mu = 0.3$), temperature range (22–50 °C), geometry, bilinear isotropic hardening material model and boundary conditions considered in this study. In particular, the weak interaction reported in (3) is established for two thermal states only and does not establish general linear additivity, which would require additional temperature levels; the thermal part of the model has not been validated against measurements, and the extreme-sliding regime lies outside the validity range of the room-temperature material parameters used. Fully predictive thermal simulation with temperature-dependent properties, cyclic analysis with kinematic or combined hardening, and sensitivity studies with respect to the principal model parameters are identified as the next necessary steps. Within these limits, the results provide a reference for wheel–rail slip damage analysis, rail-burn prevention and operational safety assessment of rail vehicles.

Author Contributions: Conceptualization, W.M. and X.S.; methodology, W.M.; software, W.M.; validation, Q.G. and T.X.; formal analysis, W.M.; investigation, Q.G. and T.X.; data curation, T.X.; writing—original draft preparation, W.M.; writing—review and editing, X.S.; visualisation, Q.G.; supervision, X.S.; project administration, X.S. All authors have read and agreed to the published version of the manuscript.

Funding: This research received no external funding.

Institutional Review Board Statement: Not applicable.

Informed Consent Statement: Not applicable.

Data Availability Statement: The data presented in this study are available on request from the corresponding authors.

Conflicts of Interest: The authors declare no conflicts of interest.

References

1. Vuković, V.; Kovalevskyy, S. Development of an innovative technical solution for the application of segmental manganese inserts on the wear surface of the clamp of the tamping railway machines. *Adv. Eng. Lett.* **2024**, *3*, 42–51. [CrossRef]
2. Meymand, S.Z.; Keylin, A.; Ahmadian, M. A survey of wheel–rail contact models for rail vehicles. *Veh. Syst. Dyn.* **2016**, *54*, 386–428. [CrossRef]
3. Wu, B.; An, B.Y.; Wen, Z.F.; Wang, W.; Wu, T. Wheel–rail low adhesion issues and its effect on wheel–rail material damage at high speed under different interfacial contaminations. *Proc. Inst. Mech. Eng. Part C J. Mech. Eng. Sci.* **2019**, *233*, 5477–5490. [CrossRef]
4. Knothe, K.; Liebelt, S. Determination of temperatures for sliding contact with applications for wheel–rail systems. *Wear* **1995**, *189*, 91–99. [CrossRef]
5. Zhao, X.; Jin, X.S.; Wen, Z.F.; Wu, L. Thermo-elastic stress of wheel–rail contact under full-slip conditions. *J. Southwest Jiaotong Univ.* **2008**, *43*, 51–56. (In Chinese) [CrossRef]

6. Wu, L.; Wen, Z.F.; Jin, X.S. Finite element model for thermo-elastic analysis of wheel–rail frictional coupling. *J. Traffic Transp. Eng.* **2007**, *7*, 21–27. (In Chinese)
7. Li, W.; Wen, Z.F.; Wu, L.; Jin, X.S. Thermo-elasto-plastic finite element analysis of rails under wheel sliding. *J. Mech. Eng.* **2010**, *46*, 95–101. (In Chinese) [CrossRef]
8. Li, W.; Wen, Z.F.; Wu, L.; Jin, X.S. Thermo-mechanical coupling analysis of rails in rolling–sliding contact. *Eng. Mech.* **2010**, *27*, 199–204. (In Chinese)
9. Naeimi, M.; Li, S.; Li, Z.; Wu, J.; Petrov, R.H.; Sietsma, J.; Dollevoet, R. Thermomechanical analysis of the wheel–rail contact using a coupled modelling procedure. *Tribol. Int.* **2018**, *117*, 250–260. [CrossRef]
10. Srivastava, J.P.; Sarkar, P.K.; Ravi Kiran, M.V.; Ranjan, V. A numerical study on effects of friction-induced thermal load for rail under varied wheel slip conditions. *Simulation* **2019**, *95*, 351–362. [CrossRef]
11. Lian, Q.; Deng, G.; Tieu, A.K.; Li, H.; Liu, Z.; Wang, X.; Zhu, H. Thermo-mechanical coupled finite element analysis of rolling contact fatigue and wear properties of a rail steel under different slip ratios. *Tribol. Int.* **2020**, *141*, 105943. [CrossRef]
12. Yang, B.; Rong, Y.X.; Yang, G.W.; Xiao, S.N.; Zhu, T. Thermo-mechanical coupling analysis of three-dimensional elastic–plastic wheel–rail sliding contact. *J. Traffic Transp. Eng.* **2022**, *22*, 208–218. (In Chinese) [CrossRef]
13. Wu, J.; Petrov, R.H.; Naeimi, M.; Li, Z.; Dollevoet, R.; Sietsma, J. Laboratory simulation of martensite formation of white etching layer in rail steel. *Int. J. Fatigue* **2016**, *91*, 11–20. [CrossRef]
14. Wang, H.H.; Wang, W.J.; Han, Z.Y.; Wang, Y.; Ding, H.H.; Lewis, R.; Lin, Q.; Liu, Q.Y.; Zhou, Z.R. Wear and rolling contact fatigue competition mechanism of different types of rail steels under various slip ratios. *Wear* **2023**, *522*, 204721. [CrossRef]
15. Wei, Y.P.; Wu, Y.P. Study on the influence of wheel–rail sliding wear on stress and temperature. *Railw. Stand. Des.* **2024**, *68*, 72–76. (In Chinese)
16. Han, F.; Li, G.M.; Wei, H.; Liu, Y.; Chen, L.; Liu, Z.L. Thermo-mechanical coupling characteristics of wheel–rail sliding contact in turnout areas. *J. China Railw. Soc.* **2025**, *47*, 113–121. (In Chinese)
17. Wei, Y.P.; Han, J.H.; Chen, Z.D. Research on the temperature rise characteristics and material fatigue damage of steel rail under different contact slip ratios. *Eng. Fail. Anal.* **2025**, *169*, 109234. [CrossRef]
18. Zhang, J.Y.; Tao, G.Q.; Wen, Z.F. Comparative analysis of wheel–rail frictional temperature rise using moving heat source and thermo-mechanical coupling methods at various wheel–rail creepages. *Proc. Inst. Mech. Eng. Part F J. Rail Rapid Transit* **2025**, *239*, 234–245. [CrossRef]
19. He, C.; Yang, Z.; Zhang, P.; Dollevoet, R.; Li, Z. Thermomechanical finite element modelling of wheel–rail contact and experimental validation. *Tribol. Int.* **2025**, *209*, 110666. [CrossRef]
20. Wei, Y.; Han, J.; Yang, T.; Wu, Y.; Chen, Z. Research on wheel/rail contact surface temperature and damage characteristics during sliding contact of a wheel. *J. Eng. Appl. Sci.* **2024**, *71*, 201. [CrossRef]
21. Li, H.; Wei, Y.; Yang, T.; Li, Y. Thermo-mechanical coupling analysis of wheel/rail contact in case of train hunting motion. *J. Eng. Appl. Sci.* **2025**, *72*, 126. [CrossRef]
22. Zhang, J.; Zuo, J. Influence of a variable friction coefficient on the thermo-mechanical behavior of railway wheel treads under different operating conditions. *Proc. Inst. Mech. Eng. Part C J. Mech. Eng. Sci.* **2026**, 09544062261472522. [CrossRef]
23. Huang, J.; Wu, B.; Xiao, G.; Shen, Q. Numerical investigation of wheel-rail adhesion using a simplified three-dimensional model considering surface roughness and temperature. *Lubr. Sci.* **2024**, *36*, 88–103. [CrossRef]
24. He, C.; Zhang, P.; Zhu, R.; Ye, R.; Li, P.; Liu, J. Experimental study of the effects of temperature and humidity on the wear and damage behavior of U71Mn rail steel. *Wear* **2023**, *524–525*, 204827. [CrossRef]
25. Zhou, L.; Hu, Y.; Ding, H.H.; Liu, Q.Y.; Guo, J.; Wang, W.J. Experimental study on the wear and damage of wheel-rail steels under alternating temperature conditions. *Wear* **2021**, *477*, 203829. [CrossRef]
26. Sahoo, S.; Singh, S.K.; Racherla, V. Estimation of rail-wheel contact forces and wear number using wheel tread temperature rise. *Proc. Inst. Mech. Eng. Part F J. Rail Rapid Transit* **2025**, *239*, 777–791. [CrossRef]
27. Tran, L.; Cookson, J.; Chiu, W.K.; Saporito, R. A review of thermal railway wheel modelling—Applicability and limitations. *Proc. Inst. Mech. Eng. Part F J. Rail Rapid Transit* **2026**, *240*, 539–554. [CrossRef]
28. Vollebregt, E.; Six, K.; Polach, O. Challenges and progress in the understanding and modelling of the wheel–rail creep forces. *Veh. Syst. Dyn.* **2021**, *59*, 1026–1068. [CrossRef]
29. Wu, L.; Wen, Z.F.; Jin, X.S. Finite element analysis of wheel/rail frictional temperature during wheel complete slides on rail. *J. Mech. Eng.* **2008**, *44*, 57–63. (In Chinese) [CrossRef]
30. Ahlström, J.; Karlsson, B. Modelling of heat conduction and phase transformations during sliding of railway wheels. *Wear* **2002**, *253*, 291–300. [CrossRef]
31. Wang, Z.; Yang, T.; Wei, Y. 3-D wheel/rail contact modeling method and temperature analyses. *Math. Models Eng.* **2025**, *11*, 47–55. [CrossRef]

32. Milojević, S.; Savić, S.; Mitrović, S.; Marić, D.; Krstić, B.; Stojanović, B.; Popović, V. Solving the problem of friction and wear in auxiliary devices of internal combustion engines on the example of reciprocating air compressor for vehicles. *Teh. Vjesn.* **2023**, *30*, 122–130. [CrossRef]
33. Ertz, M.; Knothe, K. A comparison of analytical and numerical methods for the calculation of temperatures in wheel/rail contact. *Wear* **2002**, *253*, 498–508. [CrossRef]
34. Yang, X.W.; Gu, S.J.; Zhou, S.H.; Lian, S.L. Analysis of rail thermal phase transformation induced by wheel–rail sliding contact on a 30 t axle-load heavy-haul railway. *J. China Railw. Soc.* **2016**, *38*, 84–90. (In Chinese) [CrossRef]
35. Han, J.; Wei, Y.; Yang, T. Influence of sliding wear on contact characteristics based on 3-D wheel/rail contact model. *J. Mech. Eng. Autom. Control Syst.* **2024**, *5*, 1–9. [CrossRef]
36. *TB/T 2344.1-2020*; Rails—Part 1: 43 kg/m–75 kg/m Rails. National Railway Administration: Beijing, China, 2020.
37. *TB/T 2708-2023*; Rolled Steel Integral Wheels—Passenger Cars. National Railway Administration: Beijing, China, 2023.
38. Liu, P.; Quan, Y.; Ding, G. Dynamic mechanical characteristics and constitutive modeling of rail steel over a wide range of temperatures and strain rates. *Adv. Mater. Sci. Eng.* **2019**, *2019*, 6862391. [CrossRef]
39. Johnson, K.L. *Contact Mechanics*; Cambridge University Press: Cambridge, UK, 1985. [CrossRef]
40. Roache, P.J. Perspective: A method for uniform reporting of grid refinement studies. *J. Fluids Eng.* **1994**, *116*, 405–413. [CrossRef]
41. Kim, T.-Y.; Kim, H.-K. Three-dimensional elastic-plastic finite element analysis for wheel-rail rolling contact fatigue. *Int. J. Eng. Technol.* **2014**, *6*, 1593–1600.
42. Han, F.; Wei, H.; Liu, Y. Thermal–Mechanical Coupling Analysis of Wheel–Rail Sliding Friction under Two-Point Contact Conditions. *Lubricants* **2023**, *11*, 232. [CrossRef]
43. Cooper, M.G.; Mikic, B.B.; Yovanovich, M.M. Thermal contact conductance. *Int. J. Heat Mass Transf.* **1969**, *12*, 279–300. [CrossRef]
44. Carter, F.W. On the action of a locomotive driving wheel. *Proc. R. Soc. Lond. A* **1926**, *112*, 151–157. [CrossRef]
45. Zhao, X.; Wen, Z.F.; Wang, H.Y.; Tao, G.Q.; Jin, X.S. Research progress on wheel–rail rolling contact fatigue in rail transit in China. *J. Traffic Transp. Eng.* **2021**, *21*, 1–35. (In Chinese) [CrossRef]
46. Li, Y.Q.; Zhang, Y.H.; Liu, J.P.; Zhou, S.B.; Wang, W.J. Experimental study on the wear and damage behavior of rails on heavy-haul railways. *China Railw. Sci.* **2022**, *43*, 152–160. (In Chinese) [CrossRef]
47. Ekberg, A.; Kabo, E.; Andersson, H. An engineering model for prediction of rolling contact fatigue of railway wheels. *Fatigue Fract. Eng. Mater. Struct.* **2002**, *25*, 899–909. [CrossRef]
48. Zhou, Z.; Yang, C.; Tao, G.; Wen, Z. A finite element method for reconstruction of shakedown map in wheel–rail rolling–sliding contact. *Comput. Struct.* **2025**, *319*, 107998. [CrossRef]
49. Böhmer, A.; Ertz, M.; Knothe, K. Shakedown limit of rail surfaces including material hardening and thermal stresses. *Fatigue Fract. Eng. Mater. Struct.* **2003**, *26*, 985–998. [CrossRef]
50. Ertz, M.; Knothe, K. Thermal stresses and shakedown in wheel/rail contact. *Arch. Appl. Mech.* **2003**, *72*, 715–729. [CrossRef]

Disclaimer/Publisher's Note: The statements, opinions and data contained in all publications are solely those of the individual author(s) and contributor(s) and not of MDPI and/or the editor(s). MDPI and/or the editor(s) disclaim responsibility for any injury to people or property resulting from any ideas, methods, instructions or products referred to in the content.